AN ABSTRACT OF THE DISSERTATION OF

Razvan Nes for the degree of Doctor of Philosophy in Nuclear Engineering presented on October 7, 2013.

Title: Solution of the 2D Quasi-Diffusion Low-Order Equations Using a Coupled Nodal/Finite Volume Discretization in Cartesian and Hexagonal Geometry.

Abstract approved:_____

Todd S. Palmer

An important improvement in the area of reactor core neutronic modeling is the development and use of the methods based on "quasi-diffusion" (QD) low-order equations. This family of methods takes into account the transport exactly using "functionals" computed by solving transport equations, and is amenable to solution with a variety of energy group structures and spatial discretizations. The methodology should provide transport-quality results, the only limitation being the quality of the transport-generated cross-sections and QD functionals.

The goal of this work is to develop a nodal differencing scheme for the solution of the 2-D, two-group, coarse-mesh, QD low-order equations and implement it into a code that will perform flux and k-eigenvalue calculations in Cartesian geometry and in hexagonal geometry applicable to high-temperature gas reactors. The development of the nodal differencing scheme is based on the transverse integration method. By transverse integration the 2-D problem is reduced to a 1-D problem which is then solved using a polynomial expansion of the neutron flux, fast and thermal. The QD functionals are

computed using the moments of the angular neutron flux provided by the transport code Attila. Two-group macroscopic cross-sections are extracted from the Attila output files.

The results of this research show that the effective multiplication factors with and without QD (i.e., pure diffusion) are very close due to the fact that the diagonal Eddington functionals are very close to 1/3, and the off-diagonal functionals are a few orders of magnitude smaller. The calculations have shown that the 0-th moment of the angular flux (scalar flux) is much bigger than the second moments. The analysis of the results also points out that the errors between Mathematica QD and Attila decrease with number of hexagonal nodes in zero-flux boundary condition problems and the multiplication factor for infinite-medium (zero-current boundary conditions), homogeneous problems agree much better with Attila than those with zero flux boundary conditions. This finding may suggest that the methodology that was used does not model the leakage with sufficient accuracy. The effects of the QD are small and do not seriously affect the multiplication factor in either of the geometries; however the effects are somewhat more important in Cartesian geometry compared to hexagonal geometry, presumably due to the higher symmetry of the latter.

Future research may attempt to refine the computational grid (i.e., equilateral triangles instead of entire hexagons) and/or consider different sets of expansion functions. Another area of research may involve investigating the effect of isotopic composition and the nature of the fuel and the moderator on the magnitude of the quasi-diffusion effects. Various libraries of neutron cross-sections may be explored.

Solution of the 2D Quasi-Diffusion Low-Order Equations Using a Coupled Nodal/Finite Volume Discretization in Cartesian and Hexagonal Geometry

by

Razvan Nes

A DISSERTATION

submitted to

Oregon State University

in partial fulfillment of
the requirements for the
degree of

Doctor of Philosophy

Presented October 7, 2013
Commencement June 2014

Doctor of Philosophy dissertation of Razvan Nes presented on
October 7, 2013.

APPROVED:

_____

Major Professor, representing Nuclear Engineering

_____

Head of the Department of Nuclear Engineering and Radiation Health Physics

_____

Dean of the Graduate School

I understand that my dissertation will become part of the permanent collection of Oregon State University libraries. My signature below authorizes release of my dissertation to any reader upon request.

_____

Razvan Nes, Author

ACKNOWLEDGMENTS

First and foremost I would like to express my very great appreciation to my supervising professor, Dr. Todd Palmer, for his tenacious and patient guidance throughout my entire work during the doctoral program, his careful advice, enthusiastic encouragement, and constructive critics during the materialization of this Thesis.

My grateful thanks are also extended to the software development staff of Transpire Inc., especially to Mr. Ian Davis, for their help in acquiring the license and for their willingness to give their time so generously to provide me technical support in learning to use and remotely run Attila.

I would also like to thank Mr. Aaron Bevill for the valuable help he provided me with during the early stage of the validation of the results of my research.

Special thanks to the OSU and COE Computer Support staff for making possible the remote use of the on-campus computing capabilities.

Finally I wish to thank my family for their love and unconditional support throughout my doctoral program.

TABLE OF CONTENTS

LIST OF FIGURES

LIST OF TABLES

1 INTRODUCTION

During the World War II, the research in nuclear fission was focused on achieving the capability to produce the most powerful device of destruction known to mankind, the atomic bomb, rather than harnessing the fission chain reaction with the goal of producing electric power (however, there was a certain amount of interest in using nuclear power for ship propulsion). After the end of the war, the interest in the production of electricity from controlled nuclear fission chain reaction gained importance, so by the end of the 1950's and the beginning of the 1960's the first commercial electric power plants went into operation. Ever since then, the design of the nuclear power plants has evolved in the direction of increasing the power, improving the efficiency and, very importantly, improving the safety of the power plant. Another important issue that has emerged consists in finding viable solutions for storage and disposal of the spent nuclear fuel. As of 2013, nuclear reactors generate approximately 20 percent of the United States, electrical use (NRC, 2013).

Nuclear power plants work, to some extent, by the same principle as a typical steam power plants do. Steam power plants generate electricity by the means of a generator set in motion by a steam-powered turbine. The steam is produced by heating water in a special installation: a boiler at fossil fuel power plants or nuclear reactor at nuclear power plants. Fossil fuel plants combust coal, oil, or natural gas to produce heat. Nuclear reactors produce heat by maintaining a controlled fission chain reaction. Nuclear reactors can be classified based on numerous criteria. For example, nuclear reactors can be

classified by the type of nuclear reaction, the moderator material and coolant, generation of the reactor, fuel phase, fuel type, and application.

All nuclear power reactors in the United States are fission nuclear reactors, where controlled fission chain reaction is the source of energy. The classification by type of nuclear reaction generally refers to whether the nuclear reactor uses slow (thermal) neutrons or fast neutrons. By this criterion, nuclear power reactors in the United States are in the category of thermal reactors, employing thermal neutrons. The incentive for building thermal reactors is the cost: thermal reactors are the cheapest and most common, mostly because they can use natural or low enriched uranium. In the following paragraphs we will focus on the classification of the thermal reactors.

Thermal reactors use a moderating material to slow down the neutrons from their natural energy, when ejected from broken atomic nuclei, to energies closer to the thermal energy at the temperature of the surrounding medium. Moderator material is the second classification scheme for nuclear reactors. In the United States, all nuclear power reactors use water (H_2O) as moderator. In Pressurized Water Reactors (PWR) the water is heated to extremely high temperatures, but because of the high pressure it doesn't boil. Unlike the PWRs, inside the Boiling Water Reactors (BWR) the water is heated enough by the fission process to reach its boiling point, therefore inside BWRs is a mixture of vapor and liquid water. Currently there are 104 operating nuclear power reactors in the United States: 69 PWRs and 35 BWRs (NRC, 2013), so about two-thirds of the reactors operating now in the United States are PWRs. Some thermal nuclear power reactors in

foreign countries are moderated with materials other than water, such as graphite (C) in the case of High Temperature Gas Reactors (HTGR) or heavy water (D_2O) as in the case of Canadian Deuterium Uranium (CANDU) reactors. Unlike water reactors that require uranium fuel with a concentration of the isotope U-235 higher than in natural uranium (i.e., higher than 0.72%), graphite and heavy water reactors can use natural uranium.

The agent that flows through the primary circuit and removes the heat from the reactor core where the fission reactions take place is called coolant. Different types of reactors use different types of coolant. The PWR and BWR use water as coolant, while the reactors moderated with heavy water use as coolant heavy water or water. Nuclear reactors moderated with graphite are cooled with water or a gas, typically carbon dioxide (CO_2) for older types of gas-cooled reactors or helium (He) for more advanced designs, such as HTGRs .

The classification scheme based on generations reflects the history of the development of the nuclear reactors. Generation I refers to the first reactors, most of them prototype reactors. The nuclear reactors built between the 1950s and the late 1990s for commercial use were standard-designed and are being classified as Generation II reactors. Nuclear reactors prototypical for Generation II are PWR, BWR, CANDU, and Advanced Gas-Cooled Reactors (AGR). In the late 1990s Generation III reactors came into use, more lightweight and efficient than the previous generation, as a result of designs incorporating improvements developed during the existence of Generation II of reactors. Advanced PWR, BWR, and CANDU are representative for this generation. The newest generation, Generation IV reactors, are currently in the research stage and not

expected to be in use until the late 2020s or early 2030s. Three thermal reactor designs are representative for the reactors of this generation (i) graphite-moderated helium-cooled,(ii) high-pressure, one-phase, water-moderated water-cooled, and (iii) low-pressure, graphite-moderated, molten salt-cooled, liquid fuel reactors. Higher outlet temperatures would improve thermal efficiency, and longer core life (i.e., the fuel will reside in the core for a longer period of time) will result in a smaller amount of discharged spent fuel compared to previous generations of nuclear reactors. It is, therefore, expected that these reactors will be more economical and produce minimal waste.

Most existing reactors use solid fuel; however, there are nuclear reactors designed to run on liquid or gaseous fuel. Even if U-235 is the most common nuclide in the initial nuclear fuel loads of a reactor, there are several other nuclides capable of undergoing fission that can be used to manufacture nuclear fuel. It is then reasonable to say that another type of classification is based on fuel phase (liquid, solid or gas) and fuel type. Solid fuel is most typical and consists of uranium oxide (most common) or uranium carbide, or thorium oxide or thorium carbide. Uranium and thorium are the only two reactor-ready elements available in substantial quantities on Earth. Blended with natural or depleted uranium in the so-called mixed oxide (MOX), plutonium-239, a by-product of the processes that take place in the nuclear reactors, can become fuel for thermal reactors. Currently all the power reactors in the United States are using only uranium oxide fuel. Liquid fuel typically consists of uranium or thorium tetrafluoride dissolved in molten fluoride salt flowing through a graphite reactor core that provides neutron moderation.

The energy production in gaseous fuel reactors is based on the principle of achieving criticality through compression, by external means, of uranium hexafluoride gas contained in a container placed inside a solenoid that magnetically confines the gaseous nuclear fuel. Energy is extracted directly from the plasma inside the container and from a cooling agent used to cool the container.

Based on application, reactors can be classified as: reactors for power production, propulsion, production of nuclear fuel (breeder reactors), or research reactors. Along the timeline of the development of nuclear technologies, the first reactors were built in the 1940s with the purpose of obtaining radioisotopes for military and civilian use (i.e., Plutonium-239 and medical radioisotopes). During the sixth decade of the 20th century it was proved, in several countries around the world, that nuclear reactors are a viable alternative to fossil fuels in the process of generating electric power. About the same time the United States Navy launched the first nuclear-powered submarine. Research reactors are currently used as (i) intense sources of neutrons for experiments in physics, biophysics, chemistry, non-destructive testing, etc. (ii) production of radioisotopes, (iii) testing of materials for nuclear reactors (iv) training and education.

Additional classifications, based on different criteria such as the material of the cladding or the main structural material, may be used. Nuclear power reactors currently in operation in the United States have Zircaloy for cladding and structural material. In the case of HTGR the structural material is the graphite blocks themselves.

Table 1.1 presents, for illustrative purpose, the characteristics of the two United States' reactor types, square-lattice BWR and PWR, and the HTGR (Dud 1976). In this research we used, to illustrate the hexagonal fuel assembly geometry, a reactor similar to the HTGR moderated with graphite and cooled with helium.

Table 1.1 Fuel design and operating data for, BWR and PWR, and HTGR

Assembly lattice	**BWR**	**PWR**	**HTGR**
Enrichment (% U_{235})	Low (2-5)%	Low (2-5)%	High 93%
Fuel element array	8x8	17x17	n/a
No. rods per assembly	63	264	132
Rod pitch	1.62	1.25	n/a
Assembly pitch	15.1	21.4	36.1
Pellet diameter (cm)	1.056	0.819	1.56
Moderator	water	water	graphite
Core active height x active diameter (cm x cm)	376x366	366x337	634x844

Unlike their experimental predecessors, modern nuclear power reactors are extremely complex systems. Analyzing the behavior of the reactor core requires neutron analysis computer codes coupled with thermal-hydraulic analyses of the core, structural analysis calculations, economic performance, etc. During the design of a reactor core, these calculations may be performed repeatedly.

Thermal analysis of the core gives the core size and the geometry of the lattice, while the economic performance of the core measured, for example, by the length of the fuel cycle (the length of time a fuel element can reside inside the reactor without

suffering significant structural damage) is influenced by the capability of the fuel to withstand the harsh temperature and mechanical stress conditions, as well as the intense radiation fields that induce damage to the materials utilized in the reactor core.

The negative reactivity required to ensure reactor criticality control can be distributed among several mechanisms such as movable control rods, soluble neutron poison in coolant (chemical shim), and neutron poisons that "burn out" during the reactor core life (mechanical shim). The behavior of the reactor core in interaction with these control devices requires both static and dynamic calculations.

The core neutron flux and power distributions are very important to thermal analysis and fuel depletion, and both require neutronic modeling of the entire reactor core. Radiation shielding and core multiplication factor considerations require repeated isotopic inventory and fissile material depletion over the length of the fuel cycle.

Modern nuclear reactor design depends on mathematical models implemented in computer codes. These codes simulate the neutron behavior in the reactor core. There are several types of these codes (i) cross-section library processing codes, (ii) multigroup constant generation codes, (iii) static design codes, and (iv) time-dependent design codes.

Cross-section library processing codes are complex codes that can manipulate nuclear data libraries such as ENDF/B (Dud 1976) and allow computing cross-sections for input to reactor cores.

Multigroup constant (MGC) generation codes generate few-group, average cross-sections used in design analyses. These codes provide MGCs averaged over heterogeneous regions of the reactor such as fuel assemblies or fuel cells. Such

computations require the homogenization of the heterogeneous structure of the reactor core. Homogenization techniques are generally based on disadvantage factors and collision probabilities in the thermal energy range, and self-shielding factors for the resonance integrals in the fast spectrum range. Sometimes to calculate effective homogenized cross-sections requires the use of particular techniques for the homogenization of the regions of the core within and in the proximity of strong absorbers (as in the case of control rods) (Dud 1976). In such cases, if for example diffusion theory is used, transport-corrected boundary conditions at the surface of the control rod may be used (Dud 1976).

A classification of the time-dependent design codes is given in (Dud 1976): depletion codes, fuel cycle analysis codes, and reactor kinetics analysis codes. While depletion codes are designed to model radionuclide contents of the fuel over periods of years, reactor kinetics analysis codes are dealing with events lasting minutes or less, which is the time scale of reactor transients (positive or negative insertion of reactivity).Unless more sophisticated analyses are required, depletion codes ignore the spatial distribution of the neutron flux (point reactor or zero-dimensional codes), otherwise one or two-dimensional depletion codes are used. They assume that at all times during the simulation the reactor is critical.

Static design codes utilize the MGC to actually predict the multiplication factor, neutron flux and power distribution throughout the reactor core and usually are few group, diffusion or transport codes. We will refer in more detail to these tools in the next section.

As motioned before, performing design calculations implies generating few-group cross-sections homogenized over fuel cells or entire assemblies. Modern nuclear power reactor cores contain hundreds of assemblies distributed in a pattern. To control the reactivity and the spatial power distribution some of the assemblies include control elements, which make them highly heterogeneous. The design of the controlled assemblies depends on the type of reactor (BWR, PWR, HTGR, etc). The transverse cross-section of the assemblies varies from square (BWR and PWR) to hexagonal (HTGR) or cylindrical fuel bundles (heavy water-moderated reactors). Square lattices are used in the power reactors in operation in the United States. In other countries reactor designs use also triangular lattices in hexagonal fuel assemblies. HTGR fuel assemblies include multi-coated microspheres consisting of layers of moderator around a fuel kernel, dispersed into pebbles or in cylindrical compacts/rods that are then inserted into hexagonal blocks of graphite (Sta 2007).

Stylized representations of typical BWR (a), PWR (b), and HTGR (c) fuel assemblies are presented in Figure 1.1. Note the complexity of the BWR and PWR assemblies as well as the triangular pitch and hexagonal cross-section of the HTGR fuel assembly (Sci, 2009), (Wha, 2013).

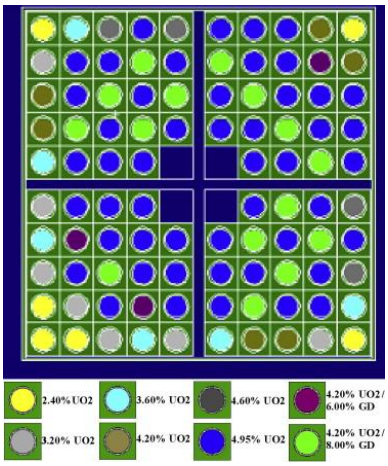

(a)

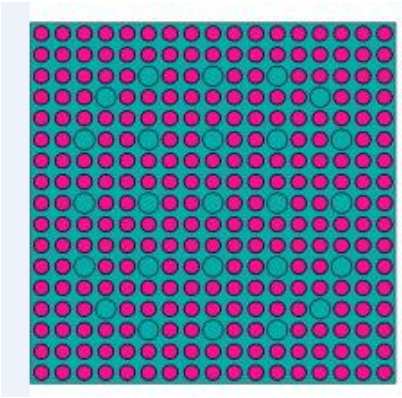

(b)

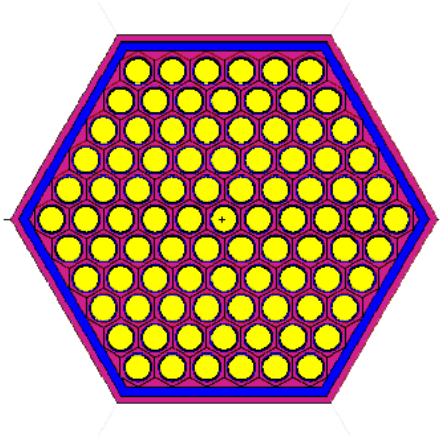

(c)

Figure 1.1 Stylized representations of typical BWR (a), PWR (b), and HTGR (c) fuel assemblies (Courtesy of ScienceDirect.com and WhatIsNuclear.com)

The current reactor physics methodology is on large scale based on two-group, nodal diffusion approximations. Nodal diffusion methods are used to calculate k-eigenvalues, and core power distributions. However, the weaknesses of the diffusion approximation are a serious limitation when highly accurate results are required. One important weakness of the diffusion-based methods is their inability to model the behavior of the neutrons at the interface between unlike fuel assemblies, such as in UO_2/MOX systems.

An important improvement is the development and use of the methods based on "quasi-diffusion" (QD) low-order equations. This family of methods takes into account the transport exactly using "functionals" computed by solving transport equations, and does not require complicated neutron energy group structure or fine-mesh spatial discretization (Ada 1994).

Most modern core analysis methods are based on solving the diffusion equation over meshes of the size of a fuel assembly - "nodal methods" (Pal 1997), (Smi 1986). Multi-dimensional diffusion equations are reduced by transverse integration (Law 1986) to a set of 1-D coupled equations. To solve these equations several methods are used: analytic methods (i.e., Analytical Nodal Method-ANM, Nodal Green's Function Method), polynomial methods (i.e., Nodal Expansion Method-NEM, QPANDA), or hybrid analytic-polynomial methods (i.e., Semi-Analytic Nodal Method-SANM used in codes such as SIMULATE-3). Other approaches use 2-D non-separable expansions of the neutron flux or interface net current moments (Pal 1997).

Among the methods used to solve the transport equation we must note one-quarter core calculations with CASMO, computer codes used for pin cell and fuel assemblies' calculations for Light Water Reactors LWR (BWR and PWR). CASMO 3, is a transport theory lattice physics computer program. CASMO 3 solves the 2-D transport equation by using the collision probability technique. Gadolinium depletion calculations are done externally, with the use of an auxiliary code. The next version, CASMO 4, is effective in computing square-lattice geometries of fuel rods of various compositions, gadolinium rods, burnable absorber rods, cluster control rods. CASMO 4 performs gadolinium depletion automatically, without any auxiliary computer code (Cor, 2006). The latest version, CASMO 5, is a state-of-the-art lattice physics code. Unlike its predecessors, CASMO 3 and CASMO 4, CASMO 5 uses the Method of Characteristics for the 2D transport solution. The method consists of tracing the tracks of the neutrons traveling through the problem, modeling the motion of the neutrons along these tracks (Stu, 2013). CASMO 5 also introduces a quadratic model for gadolinium depletion, reducing the number of time steps for depletion calculations. In addition to these features, CASMO 5 uses an improved scattering kernel in the epithermal energy range, as well as a more precise energy release model by accounting for changes that occur as lattice compositions change. CASMO 5 has proved its capability to model systems with high-concentrations of MOX and high burnable poison concentrations (Stu, 2013)

To address the limitations of single-assembly, infinite-medium transport calculations in generating physics data for smaller, highly-heterogeneous modular LWR's and non-LWR's, coarse-mesh, transport methodologies are being developed. In these

methodologies the fine-group energy structure and fine spatial discretization are replaced by equivalent few-group diffusion parameters determined for relatively large homogenized regions (called nodes) of the size of a fuel assembly (Law 1986), (Smi 1986).

The approaches to deriving the 1-D transverse integrated flux in terms of the Green's functions as basis functions instead of polynomials or other functions do not show singular terms arising from sharp changes in the surface of a node (e.g., in hexagonal geometry), but still impose the neutron balance on the flux solution (Fer 2009).

The goal of this work is to develop a nodal differencing scheme for the solution of the 2-D, two-group, coarse-mesh, QD low-order equations and implement it into a code that will perform flux and k-eigenvalue calculations in Cartesian geometry and, more importantly, a hexagonal geometry applicable to high-temperature gas reactors. The methodology should provide transport-quality results, the only limitation being the quality of the transport-generated cross-sections and QD functionals.

The implementation of the proposed QD methodology into a computer code able to accurately solve full-core problems with significantly low computational costs would be a major achievement in the field of nuclear reactor physics. Moreover, this would make it possible to upgrade the existing reactor codes for full-core calculations.

The remainder of this dissertation is organized in the following way. Chapter 2 contains a literature review briefly presenting the techniques used for solving the discrete-ordinates transport equation with emphasis on the development of the QD

method, and the existing need for codes to perform core calculations based on a hexagonal lattice. Chapter 3 contains the derivation of the QD low-order equations, the transverse-integrated form of these equations, the strategies for solving the transverse-integrated equations, and the validation of the solution strategies. In Chapter 4, we compare the results of our methodology implemented in a Mathematica code with the results of transport code Attila for one-node, four-node, and seven-node problems in hexagonal lattice geometry. The discussion of our results is presented in Chapter 5. Chapter 6 presents the conclusions of the research and potential topics for future research.

2 LITERATURE REVIEW

Spatially-differenced forms of the discrete-ordinate transport equation are usually solved by the method of iteration of the scattering source (Lew 1993), (Ada 2002). In this case the convergence of the iteration is dictated by the properties of the medium and the size of the problem. In large scattering media, where particles undergo many collisions in a single energy group and the leakage probability is small, iterative techniques converge more slowly than in small highly-absorbing systems (Lew 1993), (Ada 2002). For this reason, special iteration acceleration methods were developed.

The earliest acceleration schemes were Chebychev acceleration and fine- and coarse-mesh rebalance. Later, the research in the field followed two paths: synthetic acceleration methods and quasi-diffusion (QD) related methods (Ada 2002).

Synthetic acceleration methods are based on finding a low-order operator, similar to the original transport operator, but easier to invert. They provide additive corrections to the transport solutions generated by using the low-order operator instead of inverting the whole transport operator (Ada 2002). If derived consistently with the transport operator, the discrete low-order operator and the synthetic acceleration scheme should provide a converged solution that satisfies the transport equation regardless of the way the low-order operator was defined. An example of the low-order operator used in synthetic acceleration schemes is the diffusion operator (Ada 2002).

QD methods obtain discrete transport solutions that are influenced by the discretization of the transport and the low-order, diffusion-like, operator. QD methods are non-linear, i.e. require multiplication and division of unknowns. The low-order operator

contains transport corrections, but the quasi-diffusion-accelerated solution does not converge to the unaccelerated transport solution (Ada 2002). The advantage of the QD methods is that they provide fast convergence regardless of discretization and consistency (Ada 1994).

The QD method was developed in 1964 by Gol'din as a nonlinear method of solving the linear Boltzmann equation (Gol 1967). In the same paper, Gol'din also describes QD equations that account for anisotropy.

In 1968 Troshchiev (Tro 1968) reported consistent discretizations allowing the QD method to obtain the same solution as the unaccelerated transport equations. This made QD a true acceleration scheme (Ada 2002). Later, in 1972, Gol'din and Chetverushkin (Gol 1972) formulated the generalized QD boundary conditions, i.e. a general relationship between flux and current that involves QD coefficients calculated using the angular flux from a previous transport sweep. To be more specific, the paper (Gol 1972) explains a method of solving the 1-D cylindrical geometry gas dynamics equations. The unknown for which the transport equation is solved is intensity, and the boundary conditions relate the radiative energy flux to the energy density of the radiation by the means of QD coefficients.

In 1978, Aksenov and Gol'din (Aks 1979) successfully performed 2-D QD calculations of neutron transport, demonstrating the applicability of the method in two-dimensional problems.

In 1982, Gol'din formulated abstractly the QD method, and applied it to multigroup neutron transport problems with anisotropic scattering (Ada 2002). The

effects of various spatial discretizations of the transport equation given a constant low-order equation discretization were analyzed, in 1986, by Anistratov and Gol'din (Ada 2002).

Later, Miften and Larsen (Mif 1993) developed a symmetric QD method (SQD) that yields an "accurate and efficiently solvable" discretization of multidimensional transport problems. This method combines the advantages of QD methods (i.e. no consistent discretization required) with the convenience of solution by the standard conjugate gradient method; in addition to this, the SQD can be more easily generalized to nonorthogonal grids than the discretized synthetic acceleration technique.

In 1986 and later, in 1996, Gol'din used QD to solve coupled material-temperature and radiative transfer equations (Ada 2002). The QD method applied to anisotropic scattering problems described by Gol'din (Gol 1967) was implemented in the late 1990s for strongly anisotropic scattering (Ada 2002). In 1993 Aristova developed a finite difference scheme for the QD elliptic operator in oblique-angle cells with applications in studying high-temperature radiative gas dynamics (Ari 1993).

Soon after the QD method was created by Gol'din in 1964, nonlinear QD-related methods were derived by Nikolaishvilli ("Yves-Mertens" approximation in 1966), Germogenova ("Method of average fluxes" in 1968), and Gol'din himself in 1969. In 1970 Gol'din extended these methods to electron transport problems. Notable contributions in QD-related methods are due to Anistratov and Larsen (Weighted alpha methods in 1996 and 2001) (Ada 2002).

An advanced discretization scheme, described by Palmtag (Pal 1997), was applied by Nes and Palmer to solve the 2-D, low-order, QD equations for constant QD functionals (Nes 2002).

In 2003, Hiruta, Anistratov, and Adams presented an efficient method of solving QD low-order equations based on splitting the problem into a space-constant QD functional problem over the interior region of a fuel assembly and a strong space-dependent QD functional problem near the assembly boundaries (Hir 2003).

A methodology for including the dissimilar neighbors on a given assembly's parameters in single-assembly transport calculations was developed by Clarno and Adams (Cla 2003).

Advances in the analysis of Liquid Metal Fast Breeder Reactors-LMFBR, High Temperature Gas-Cooled Reactors-HTGR, prismatic Very-High Temperature Reactors-VHTR, and other reactors with hexagonal lattices have led the research in the direction of developing techniques of solving the neutron diffusion equation in 2-D and 3-D, hexagonal geometry.

Conventional finite-difference techniques using uniform triangular grids applied within each hexagonal fuel assembly were initially used in global core calculations for hexagonal lattices. Successful use of nodal methods in Cartesian geometry has led to analogous formulations that can be directly applied to hexagonal meshes.

A transverse-integrated polynomial nodal expansion method applied to neutron diffusion in hexagonal geometry is presented by Lawrence and is implemented in the DIF3D code (Law 1883), (Law 1986). In hexagonal geometry, because of the sharp

changes in the surface of a hexagon at the vertices, transverse leakage terms include singular terms. This issue is addressed by Lawrence by including discontinuous polynomial expansion functions. Due to discontinuous polynomial approximations, Lawrence's nodal expansion method in hexagonal geometry is not as accurate as it is for Cartesian geometry.

Other proposed methods in hexagonal geometry are based on nodal Green's functions and avoid the discontinuous leakage terms, but impose a neutron balance on the flux solution which recovers the leakage terms (Fer 2009). A nodal triangular z-polynomial expansion method – TPEN on uniform triangular nodes, using a non-separable 2-D polynomial function expansion of the neutron flux, is implemented in computer codes such as PARCS (Pal 2009, private communication). The Raviat-Thomas method is applied to the solution of the diffusion equation in Cartesian geometries and, with suitable transformation of the polynomial basis, in hexagonal geometries (Heb 2007).

3 METHODS

This chapter describes the methodology for solving the QD low-order equations in Cartesian and hexagonal geometry. The chapter starts by briefly describing the derivation of the QD low-order equations, their nodal discretization in Cartesian and hexagonal geometry. In the following sections we describe the transverse-integrated form of the QD equations together with the strategy for finding their solution in Cartesian and hexagonal geometry. In the final sections of the chapter we show our solution strategies applied to a number of problems for the purpose of their validation.

3.1 The Quasi-diffusion Method for Neutron Transport

The QD method for solving the transport equation consists of reducing the dimensionality of the problem by averaging the transport equation over the angular and energy variables. The QD system of equations includes special functionals that depend weakly on the transport problem solution (QD functionals, or Eddington tensor). The result is a nonlinear QD problem, equivalent to the original linear transport problem. In the following sections we show how this methodology can be successfully implemented into two-group, coarse-mesh, diffusion-like codes.

3.1.1 The low-order quasi-diffusion equations

Consider the k-eigenvalue neutron transport equation with isotropic scattering in the multigroup formulation (Lew 1993), (Dud 1976),

$$\hat{\Omega}\bullet\nabla\psi_g(\hat{r},\hat{\Omega})+\Sigma_g(\hat{r})\psi_g(\hat{r},\hat{\Omega})=\frac{1}{4\pi}\sum_{g'=1}^{G}\Sigma_{g'g}(\hat{r})\Phi_{g'}(\hat{r})+$$
$$+\frac{\chi_g}{4\pi k}\sum_{g'=1}^{G}\upsilon\Sigma_{fg'}(\hat{r})\Phi_{g'}(\hat{r}) \quad . \qquad (3.1)$$

where

- $\hat{\Omega}$ is the direction,
- $\psi_g(\hat{r},\hat{\Omega})$ is the angular flux,
- $\Sigma_g(\hat{r})$ is the total cross-section for neutrons in group g,
- $\Sigma_{g'g}(\hat{r})$ is the scattering cross-section for neutrons between groups g' and g,
- $\Phi_{g'}(\hat{r})$ is the scalar flux in group g',
- χ_g is the fission neutron spectrum,
- k is the multiplication factor,
- υ is the number of neutrons per fission, and
- $\Sigma_{fg'}(\hat{r})$ is the fission cross-section for neutrons in group g'.

The scalar neutron flux in group g is defined as follows (Lew 1993), (Dud 1976)

$$\Phi_g(\hat{r})=\int_{4\pi}\psi_g(\hat{r},\hat{\Omega})d\Omega \qquad (3.2)$$

and the component *i (i=x,y,z)* of the neutron current, in group g is given by

$$\int_{4\pi}d\hat{\Omega}\Omega_i\psi_g(\hat{r},\hat{\Omega})=J_{gi}(\hat{r}) \qquad (3.3)$$

One demonstrates (Mif 1993) that, after algebraic manipulations, from equation (3.1) two other equations can be derived. The first is a balance equation for neutrons in group *g*

$$\nabla \bullet \hat{\mathrm{J}}_{\mathrm{g}}(\hat{r}) + \Sigma_{rg}(\hat{r})\Phi_g(\hat{r}) = \sum_{\substack{g'=1 \\ g' \neq g}}^{G} \Sigma_{g'g}(\hat{r})\Phi_{g'}(\hat{r}) + \frac{\chi_g}{k}\sum_{g'=1}^{G} \upsilon\Sigma_{fg'}(\hat{r})\Phi_{g'}(\hat{r}). \qquad (3.4)$$

and the other is a diffusion-like equation that relates the components of the current to neutron flux

$$\nabla(E_{gij}(\hat{r})\Phi_g(\hat{r})) + \Sigma_g(\hat{r})J_{gi}(\hat{r}) = 0 \qquad (3.5)$$

In (3.5) the new quantities

$$E_{gij}(\hat{r}) = \frac{\int_{4\pi} \Omega_i \Omega_j \psi_g(\hat{r},\hat{\Omega}) d\Omega}{\int_{4\pi} \psi_g(\hat{r},\hat{\Omega}) d\Omega} \quad \text{for i,j=x,y,z} \qquad (3.6)$$

are the QD functionals (or, Eddington functionals).

In (3.4) a "removal" cross-section was defined such as

$$\Sigma_{rg}(\hat{r}) = \Sigma_g(\hat{r}) - \Sigma_{gg}(\hat{r}) \qquad (3.7)$$

The QD functionals (3.6) are the components of a positive-definite tensor and are weakly dependent on position (Hir 2003). It can be shown (Lew 1993) that if the angular flux is a linear function of angle, the diagonal components of the Eddington tensor equal 1/3, the off-diagonal components equal 0, and (3.5) takes the form of Fick's law.

3.1.2 Nodal discretization of the low-order quasi-diffusion equations

Considering the 2-D, low-order QD equations, the problem domain is created by dividing the x-y plane into non-overlaping nodes of square or hexagonal shape.

3.1.2.1 Cartesian geometry

Square nodes are shown in Fig. 3.1. The dimensions of a square node are ±h/2, as depicted in the figure. The neutron fluxes and currents at the faces of the node are marked as follows: plus (+) for the right and top faces and minus (-) for the left and bottom faces, respectively.

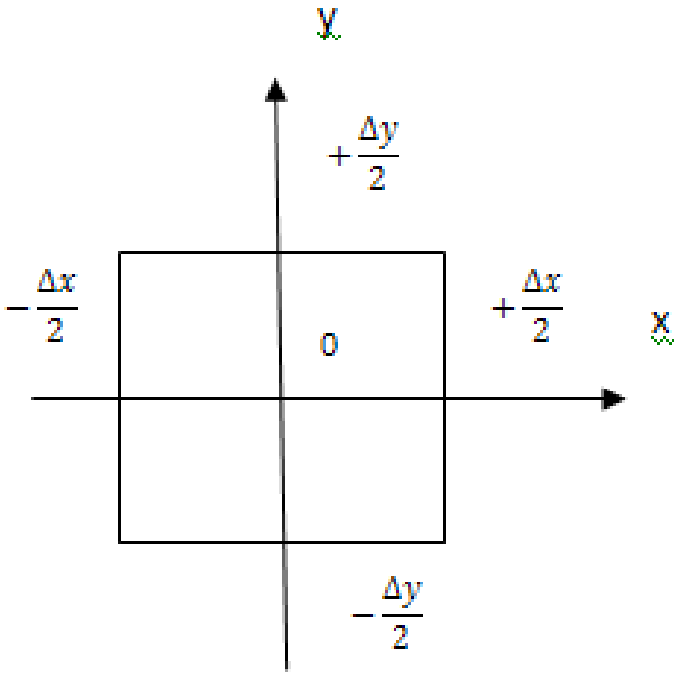

Figure 3.1 Standard Cartesian coordinates

3.1.2.2 Hexagonal geometry

Hexagonal node geometry and coordinates are illustrated in Fig. 3.2. The *u* and *v* directions are defined perpendicular on two adjacent faces of the hexagonal node. Positive and negative directions are denoted by plus (+) and minus (-), respectively.

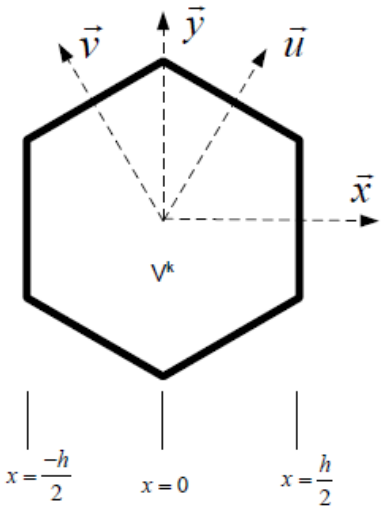

Figure 3-2 Standard hexagonal coordinates (Fer 2009).

The distance between two opposite faces of the hexagonal node is denoted by *h* ("flat-to-flat distance"). The equations of the hexagonal node surfaces normal to *u* and *v* directions are $y_s(x) = \frac{1}{\sqrt{3}}(h - |x|)$.

3.1.3 Solution Strategies

The dimensionality of the QD problems can be reduced from 2-D to 1-D by integrating the equation over one of the dimensions. In the following sections we integrate the 2-D problems over y, and the newly-obtained equations are in the x-variable, being then solved by the method of weighted residuals.

3.1.3.1 Transverse integration method in Cartesian geometry

The approach we take in solving the low-order quasi-diffusion equations is the transverse integration method proposed by Lawrence (Law 1986). In 2-D, Cartesian geometry, equation (3.4) takes the form:

$$\frac{\partial}{\partial x}J_{gx}(x,y)+\frac{\partial}{\partial y}J_{gy}(x,y)+\Sigma_{gr}(x,y)\Phi_{g}(x,y)=\sum_{\substack{g'=1\\ g'\neq g}}^{G}\Sigma_{g'g}(x,y)\Phi_{g'}(x,y)+\frac{\chi_g}{k}\sum_{g'=1}^{G}\upsilon\Sigma_{fg'}(x,y)\Phi_{g'}(x,y) \qquad (3.8)$$

For two energy groups *g=1* (fast) and *g=2* (thermal) and node-averaged neutron cross-sections, equation (3.8) become

$$\frac{\partial}{\partial x}J_{1x}(x,y)+\frac{\partial}{\partial y}J_{1y}(x,y)+\Sigma_{1r}\Phi_{1}(x,y)=\frac{1}{k}\sum_{g'=1}^{2}\upsilon\Sigma_{fg'}\Phi_{g'}(x,y) \qquad (3.9)$$

$$\frac{\partial}{\partial x}J_{2x}(x,y)+\frac{\partial}{\partial y}J_{2y}(x,y)+\Sigma_{2r}\Phi_{2}(x,y)=\Sigma_{12}\Phi_{1}(x,y), \qquad (3.10)$$

where we have assumed that all the neutrons produced by fission have energies in the fast group.

By integrating equations (3.9) and (3.10) over the node volume $V = \Delta x\Delta y$ we obtained the "balance equations" for the node :

$$\frac{1}{\Delta x}\left[J_{1x+}-J_{1x-}\right]+\frac{1}{\Delta y}\left[J_{1y+}-J_{1y-}\right]+\Sigma_{1r}\overline{\Phi}_{1}=\frac{1}{k}\sum_{g'=1}^{2}\upsilon\Sigma_{fg'}\overline{\Phi}_{g'} \qquad (3.11)$$

$$\frac{1}{\Delta x}\left[J_{2x+}-J_{2x-}\right]+\frac{1}{\Delta y}\left[J_{2y+}-J_{2y-}\right]+\Sigma_{2r}\overline{\Phi}_{2}=\Sigma_{12}\overline{\Phi}_{1}, \qquad (3.12)$$

where

$$\overline{\Phi}_g = \frac{1}{\Delta x \Delta y}\int_{-\Delta y/2}^{\Delta y/2} dy \int_{-\Delta x/2}^{\Delta x/2} dx \Phi_g(x,y), \tag{3.13}$$

$$J_{gx\pm} = \frac{1}{\Delta y}\int_{-\Delta y/2}^{\Delta y/2} dy \left[J_g(x,y) \right]_{x \to \pm \Delta x/2}, g = 1,2. \tag{3.14}$$

Nearly all recent nodal methods are based on approximations of multidimensional equations by 1-D equations by integrating the equation over the direction(s) transverse to each coordinate axis (Law 1986). For example, the x-direction equation can be obtained by integrating equations (3.9) and (3.10) over the y-direction:

$$\frac{d}{dx}\overline{J}_{1x}(x) + \Sigma_{1r}\overline{\Phi}_1(x) = \frac{1}{k}\sum_{g'=1}^{2} \upsilon\Sigma_{fg'}\overline{\Phi}_{g'}(x) - \frac{1}{\Delta y}\left[J_1(x, \Delta y/2) - J_1(x, -\Delta y/2) \right] \tag{3.15}$$

$$\frac{d}{dx}\overline{J}_{2x}(x) + \Sigma_{2r}\overline{\Phi}_2(x) = \Sigma_{12}\overline{\Phi}_1(x) - \frac{1}{\Delta y}\left[J_2(x, \Delta y/2) - J_2(x, -\Delta y/2) \right], \tag{3.16}$$

where

$$\overline{\Phi}_g(x) = \frac{1}{\Delta y}\int_{-\Delta y/2}^{\Delta y/2} dy \Phi_g(x,y), \tag{3.17}$$

$$J_{gx} = \frac{1}{\Delta y}\int_{-\Delta y/2}^{\Delta y/2} dy J_g(x,y), g = 1,2. \tag{3.18}$$

3.1.3.2 Neutron flux expansion in Cartesian geometry

Both transverse-integrated fast and thermal neutron fluxes are represented as 1-D expansions of polynomial functions. The polynomial basis functions are identical for the

fast and the thermal flux expansions. For example, the y-integrated flux expansion in quartic polynomial basis functions is:

$$\overline{\Phi}_{gx}(x) = \overline{\Phi}_g f_0(x) + \sum_{n=1}^{4} a_{gxn} f_n(x)$$
$$x \in \left[-\Delta x/2, +\Delta x/2\right] \tag{3.19}$$

where *g=1,2* for fast and thermal neutron flux, respectively. The first expansion coefficient is $\overline{\Phi}_g$, the node-averaged flux (*g=1,2*).

The polynomial basis functions in (3.19) are given by Lawrence (Law 1986):

$$\begin{aligned} f_0(\xi) &= 1, \\ f_1(\xi) &\equiv \frac{x}{\Delta x} \equiv \xi, \\ f_2(\xi) &= 3\xi^2 - \frac{1}{4}, \\ f_3(\xi) &= \xi(\xi + \frac{1}{2})(\xi - \frac{1}{2}), \\ f_4(\xi) &= (\xi^2 - \frac{1}{20})(\xi + \frac{1}{2})(\xi - \frac{1}{2}). \end{aligned} \tag{3.20}$$

Polynomial basis functions (3.20) are represented in the plot in Figure 3.3.

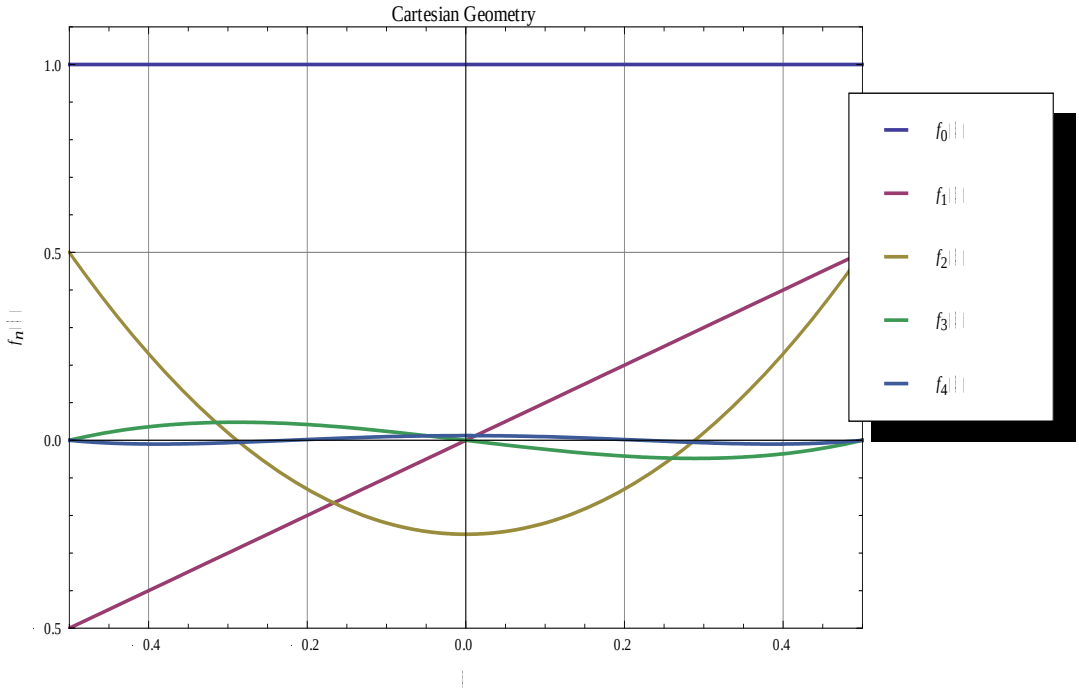

Figure 3.3 Quartic polynomial expansion functions in Cartesian geometry

3.1.3.3 Solution of the transverse-integrated equations in Cartesian geometry

As a result of the particular form of the high-order expansion functions, the low-order expansion coefficients and the node-averaged and face-averaged fluxes are related as follows:

$$a_{gx1} = \Phi_{gx+} - \Phi_{gx-} \tag{3.21}$$

$$a_{gx2} = \Phi_{gx+} + \Phi_{gx-} - 2\overline{\Phi}_g \tag{3.22}$$

The expansion (3.19) of the flux has 5 non-zero coefficients. Finally, one must solve for 9 unknown expansion coefficients per node, per group: $\overline{\Phi}_g$, a_{gxn}, and a_{gyn},where $n=1,4$ and $g=1,2$.

In general, the linear system contains the following 18 equations per node (Law 1986):

- 1 “balance equation” in the fast group
- 1 “balance equation” in the thermal group
- 2 weighted “residual moments” in the fast group
- 2 weighted “residual moments” in the thermal group
- 2 equations for the outgoing partial surface-averaged currents at the surfaces of the node in the fast group
- 2 equations for the outgoing partial surface-averaged currents at the surfaces of the node in the thermal group
- 4 surface-averaged (dis)continuity conditions in the fast group
- 4 surface-averaged (dis)continuity conditions in the thermal group

The two weight functions that are used to calculate the weighted residual moments and the higher-order coefficients of the polynomial flux expansion are chosen from the basis functions (3.20). Numerical studies have shown that lower order weight functions yield superior accuracy (Law 1986), therefore $f_1(x)$ and $f_2(x)$ were selected as weight functions:

$$w_1(x) = f_1(x) = x, \tag{3.23}$$

$$w_2(x) = f_2(x) = 3x^2 - \frac{1}{4}. \tag{3.24}$$

To apply the weighted residual procedure to equations (3.15) and (3.16) we multiply the equation by the weight functions and integrate over $[-\Delta x/2, +\Delta x/2]$:

$$\langle w_n(x), \frac{d}{dx}\bar{J}_{1x}(x)\rangle + \Sigma_{1r}\bar{\Phi}_{1xn} = \frac{1}{k}\sum_{g'=1}^{2}\upsilon\Sigma_{fg'}\bar{\Phi}_{g'xn} - \langle w_n(x), \frac{1}{\Delta y}\left[J_1(x,\Delta y/2) - J_1(x,-\Delta y/2)\right]\rangle \quad (3.25)$$

$$\langle w_n(x), \frac{d}{dx}\bar{J}_{2x}(x)\rangle + \Sigma_{2r}\bar{\Phi}_{2xn} = \Sigma_{12}\bar{\Phi}_{1xn} - \langle w_n(x), \frac{1}{\Delta y}\left[J_2(x,\Delta y/2) - J_2(x,-\Delta y/2)\right]\rangle, \quad (3.26)$$

where the inner products are

$$\langle w_n(x), \frac{d}{dx}\bar{\Phi}_{gx}(x)\rangle = \bar{\Phi}_{gxn} = \frac{1}{\Delta x}\int_{-\Delta x/2}^{\Delta x/2} dx w_n(x)\bar{\Phi}_{gx}(x), \quad (3.27)$$

$$\langle w_n(x), \frac{d}{dx}\bar{J}_{2x}(x)\rangle = \frac{1}{\Delta x}\int_{-\Delta x/2}^{\Delta x/2} dx w_n(x)\frac{d}{dx}\bar{J}_{2x}(x). \quad (3.28)$$

Equations (3.27) and (3.28) are the node-averaged moments of the neutron flux and the current in the *x*-direction.

The first weighted moment of equations (3.15) and (3.16) are derived from (3.25) and (3.26) using $w_1(x)$ given by (3.23):

$$\frac{1}{2}\frac{1}{\Delta x}\left[J_{1x+} + J_{1x-}\right] + \frac{1}{\Delta x}\frac{1}{\Delta x}\frac{E_{1xx}}{\Sigma_{1t}}a_{1x1} + \Sigma_{1r}\bar{\Phi}_{1x1} = \frac{1}{k}\sum_{g'=1}^{2}\upsilon\Sigma_{fg'}\bar{\Phi}_{g'x1} - \frac{1}{\Delta y}L_{1y1}, \quad (3.29)$$

$$\frac{1}{2}\frac{1}{\Delta x}\left[J_{2x+} + J_{2x-}\right] + \frac{1}{\Delta x}\frac{1}{\Delta x}\frac{E_{2xx}}{\Sigma_{2t}}a_{2x1} + \Sigma_{2r}\bar{\Phi}_{2x1} = \Sigma_{12}\bar{\Phi}_{1x1} - \frac{1}{\Delta y}L_{2y1} \quad (3.30)$$

The first weighted moment of equations (3.15) and (3.16) are derived from (3.25) and (3.26) using $w_2(x)$ given by (3.24) and the current given by (3.5):

$$\frac{1}{2}\frac{1}{\Delta x}\left[J_{1x+} - J_{1x-}\right] + \frac{3}{\Delta x}\frac{1}{\Delta x}\frac{E_{1xx}}{\Sigma_{1t}}a_{1x2} + \Sigma_{2r}\bar{\Phi}_{1x1} = \frac{1}{k}\sum_{g'=1}^{2}\upsilon\Sigma_{fg'}\bar{\Phi}_{g'x2} - \frac{1}{\Delta y}L_{1y2}, \quad (3.31)$$

$$\frac{1}{2}\frac{1}{\Delta x}\left[J_{2x+} - J_{2x-}\right] + \frac{3}{\Delta x}\frac{1}{\Delta x}\frac{E_{2xx}}{\Sigma_{2t}}a_{2x2} + \Sigma_{2r}\bar{\Phi}_{2x2} = \Sigma_{12}\bar{\Phi}_{1x2} - \frac{1}{\Delta y}L_{2y2} \quad (3.32)$$

With these preparations, the high-order expansion coefficients are obtained from (3.21), (3.22), and (3.29)-(3.32):

$$a_{gx3} = -120\Phi_{gx1} + 10a_{gx1} \tag{3.33}$$

$$a_{gx4} = -700\Phi_{gx2} + 35a_{gx2} \tag{3.34}$$

Additional approximations for the transverse leakage terms and their moments are required to solve for the expansion coefficients. An approximation in which transverse leakage in the *y*-direction is represented by a quadratic polynomial in *x* is described in (Law 1986). In this case, the basis functions are the first three expansion functions of (3.20). One could set the coefficients of $f_1(x)$ and $f_2(x)$ to zero, in which case the leakage term moments are zero (flat transverse leakage approximation).

In the approximation of the quadratic transverse leakage, assuming that the leakage is satisfactory described by a quadratic polynomial over three consecutive nodes (equation 3.35), one can distinguish three situations. The objective of this derivation is finding the coefficients of the quadratic expansion. There are three cases that may apply in practice. In the first case, also known as the central node scheme, the reference node *k* is the central node, accompanied by the nodes at the left and the right, respectively. In the second case, the forward case, the reference node *k* is the leftmost node, accompanied by the next two nodes to the right. The third case, the backward case, the reference node *k* is the rightmost node, accompanied by the previous two nodes to the left.

$$L_{gy}^{k}(x) = L_{gy}^{k} + \rho_{g1y}^{k} u + \rho_{g2y}^{k}(3u^2 - \frac{1}{4}) \tag{3.35}$$

where L_{gy}^{k} is the average transversal leakage rate from node *k* and ρ_{g1y}^{k} and ρ_{g2y}^{k} are the coefficients of the quadratic expansion of the transverse leakage from node *k.*

In the following paragraphs we describe the methodology of derivation of the transverse leakage rates in the central, forward, and backwards schemes, as shown in Figures 3.4, 3.5, and 3.6. In all three cases, the x-axis positive direction is in the direction the node indexes increase: *(k-2), (k-1), (k), (k+1)* and *(k+2).*

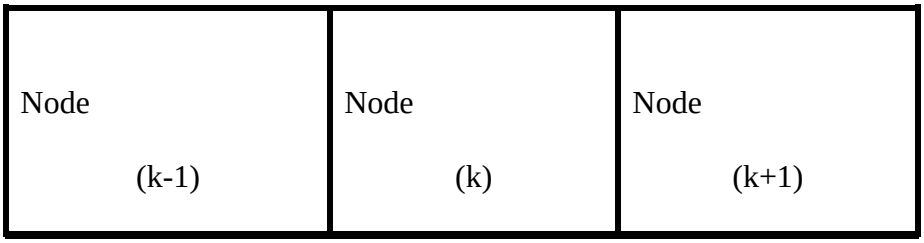

Figure 3.4 Central scheme

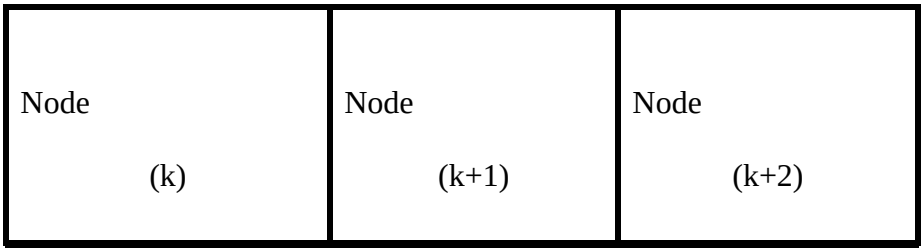

Figure 3.5 Forward scheme

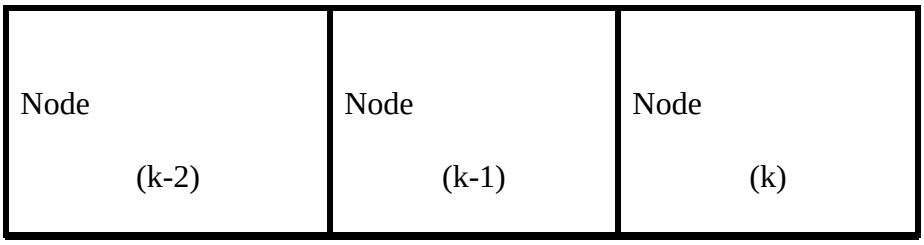

Figure 3.6 Backward scheme

Central node scheme

In the Central node scheme the average transverse leakage rates of the adjacent nodes *k-1* and *k+1* are given by

$$L_{gy}^{k-1} = L_{gy}^{k} + \rho_{g1y}^{k}\int_{-3/2}^{-1/2} u\,du + \rho_{g2y}^{k}\int_{-3/2}^{-1/2}(3u^2 - \frac{1}{4})du$$
$$L_{gy}^{k+1} = L_{gy}^{k} + \rho_{g1y}^{k}\int_{1/2}^{3/2} u\,du + \rho_{g2y}^{k}\int_{1/2}^{3/2}(3u^2 - \frac{1}{4})du \qquad (3.36)$$

Solving for ρ_{g1y}^{k} and ρ_{g2y}^{k} gives the coefficients of the quadratic expansion of the transverse leakage rates on the y direction in terms of $L_{gy}^{k-1}, L_{gy}^{k}, L_{gy}^{k+1}$,

$$\rho_{g1y}^{k} = \frac{1}{2}(L_{gy}^{k+1} - L_{gy}^{k-1})$$
$$\rho_{g2y}^{k} = \frac{1}{6}(L_{gy}^{k+1} - 2L_{gy}^{k} + L_{gy}^{k-1}) \qquad (3.37)$$

Forward scheme

In this scheme we move from node *k* to the next nodes *k+1* and *k*+2. The average transverse leakage rates of the adjacent nodes *k+1* and *k+2* are given by

$$L_{gy}^{k+1} = L_{gy}^{k} + \rho_{g1y}^{k}\int_{1/2}^{3/2} u\,du + \rho_{g2y}^{k}\int_{1/2}^{3/2}(3u^2 - \frac{1}{4})du$$
$$L_{gy}^{k+2} = L_{gy}^{k} + \rho_{g1y}^{k}\int_{3/2}^{5/2} u\,du + \rho_{g2y}^{k}\int_{3/2}^{5/2}(3u^2 - \frac{1}{4})du \qquad (3.38)$$

Solving for $\rho_{g1y}^{k}\ and\ \rho_{g2y}^{k}$ gives the coefficients of the quadratic expansion of the transverse leakage rates on the y direction in terms of , $L_{gy}^{k}, L_{gy}^{k+1}, L_{gy}^{k+2}$,

$$\rho_{g1y}^{k} = \frac{1}{2}(4L_{gy}^{k+1} - 3L_{gy}^{k} - L_{gy}^{k+2})$$
$$\rho_{g2y}^{k} = \frac{1}{6}(L_{gy}^{k+2} - 2L_{gy}^{k+1} + L_{gy}^{k}) \tag{3.39}$$

Backward scheme

In the Backward scheme we move backwards from node *k* to nodes *(k-1)* and *(k-2)*. The average transverse leakage rates of the adjacent nodes *k-2* and *k-1* are given by

$$L_{gy}^{k-1} = L_{gy}^{k} + \rho_{g1y}^{k}\int_{-3/2}^{-1/2} u du + \rho_{g2y}^{k}\int_{-3/2}^{-1/2}(3u^2 - \frac{1}{4})du$$
$$L_{gy}^{k-2} = L_{gy}^{k} + \rho_{g1y}^{k}\int_{-5/2}^{-3/2} u du + \rho_{g2y}^{k}\int_{-5/2}^{-3/2}(3u^2 - \frac{1}{4})du \tag{3.40}$$

Solving for $\rho_{g1y}^{k}\ and\ \rho_{g2y}^{k}$ gives the coefficients of the quadratic expansion of the transverse leakage rates on the y direction in terms of $L_{gy}^{k}, L_{gy}^{k-1}, L_{gy}^{k-2}$,

$$\rho_{g1y}^{k} = \frac{1}{2}(3L_{gy}^{k+1} - 4L_{gy}^{k} - L_{gy}^{k-2})$$
$$\rho_{g2y}^{k} = \frac{1}{6}(L_{gy}^{k-2} - 2L_{gy}^{k-1} + L_{gy}^{k}) \tag{3.41}$$

Partial surface-averaged QD currents at the left and right x-directed surfaces of the node are obtained as follows:

$$J_{gx+}^{out} = -\frac{1}{\Delta x}\frac{E_{gxx}}{\Sigma_{gt}}\left[a_{gx1} + 3a_{gx2} + \frac{1}{2}a_{gx3} + \frac{1}{5}a_{gx4}\right] - \frac{1}{\Delta x}\frac{E_{gxy}}{\Sigma_{gt}}a_{gy1} + J_{gx+}^{in} \tag{3.42}$$

$$J_{gx-}^{out} = +\frac{1}{\Delta x}\frac{E_{gxx}}{\Sigma_{gt}}\left[a_{gx1} - 3a_{gx2} + \frac{1}{2}a_{gx3} - \frac{1}{5}a_{gx4}\right] - \frac{1}{\Delta x}\frac{E_{gxy}}{\Sigma_{gt}}a_{gy1} + J_{gx-}^{in} \tag{3.43}$$

In deriving equations (3.41) and (3.42) we assumed in the QD equation (3.5) a multidimensional expansion in quartic polynomials of the form

$$\begin{aligned}&\overline{\Phi}_{gx}(x) = \overline{\Phi}_g f_0(x) + \sum_{n=1}^{4} a_{gxn} f_n(x) + \sum_{n=1}^{4} a_{gyn} f_n(y),\\ &x \in \left[-\Delta x/2, +\Delta x/2\right], y \in \left[-\Delta y/2, +\Delta y/2\right],\end{aligned} \tag{3.44}$$

3.1.3.4 Transverse integration method in hexagonal geometry

We consider a 2-D hexagonal geometry, where the node is defined in terms of local *(x,y)* coordinates as shown in Fig. 3.2,

$$\begin{aligned}&x \in [-h/2, +h/2], y \in [-y_s(x), +y_s(x)],\\ &y_s(x) = \frac{1}{\sqrt{3}}(h - |x|)\end{aligned} \tag{3.45}$$

where h is the hexagonal lattice pitch, i.e. the distance between two opposite sides of the hexagon.

The one-dimensional flux (Law 86), analogous to equation (3.17) is

$$\overline{\Phi}_g(x) = \frac{1}{2y_s(x)}\int_{-y_s(x)}^{y_s(x)} dy \Phi_g(x, y). \tag{3.46}$$

Because of the dependence of the y-direction mesh spacing upon x, it is more convenient to work with the partially-integrated flux and current (Law 86):

$$\Phi_g(x) = \int_{-y_s(x)}^{y_s(x)} dy \Phi_g(x,y). \tag{3.47}$$

$$J_{gx}(x) = \int_{-y_s(x)}^{y_s(x)} dy J_g(x,y), g = 1,2 \tag{3.48}$$

Two similar integrated fluxes and currents are defined for the other pairs of opposite faces of the hexagonal node.

The transverse integrated diffusion equation is derived performing a neutron balance equation over the vertical stripe $x \in [x, x+dx], y \in [-y_s(x), +y_s(x)]$ and the result is

$$\frac{d}{dx} J_{1x}(x) + \Sigma_{1r} \Phi_1(x) = \frac{1}{k} \sum_{g'=1}^{2} \upsilon \Sigma_{fg'} \Phi_{g'}(x) - \frac{2}{\sqrt{3}} \left[J_1\left(x, +y_s(x)\right) - J_1\left(x, -y_s(x)\right) \right] \tag{3.49}$$

$$\frac{d}{dx} J_{2x}(x) + \Sigma_{2r} \Phi_2(x) = \Sigma_{12} \Phi_1(x) - \frac{2}{\sqrt{3}} \left[J_2\left(x, +y_s(x)\right) - J_2\left(x, -y_s(x)\right) \right], \tag{3.50}$$

where $J_g\left(x, \pm y_s(x)\right), g = 1,2,$ are the surface-normal currents across the *u*- and *v*-directed faces (Law 1986).

3.1.3.5 Neutron flux expansion in hexagonal geometry

In hexagonal geometry, the partially-integrated flux in the *x* direction is approximated by (Law 1983)

$$\Phi_{gx}(x) = 2y_s(x)[\overline{\Phi}_g + \sum_{n=1}^{4} a_{gxn} f_n(x)], \tag{3.51}$$

where

$$f_1(\xi) = \frac{x}{h} = \xi,$$
$$f_2(\xi) = \frac{36}{13}\xi^2 - \frac{5}{26},$$
$$f_3(\xi) = \frac{10}{13}\xi^2 - \frac{1}{2}|\xi| + \frac{3}{52},$$
$$f_4(\xi) = \xi(|\xi| - \frac{1}{2}).$$

Expansions similar to (3.44) apply to partially-integrated fluxes along the u- and v- directions. The expansion functions for the hexagonal geometry are presented in the plot illustrated in Figure 3.7.

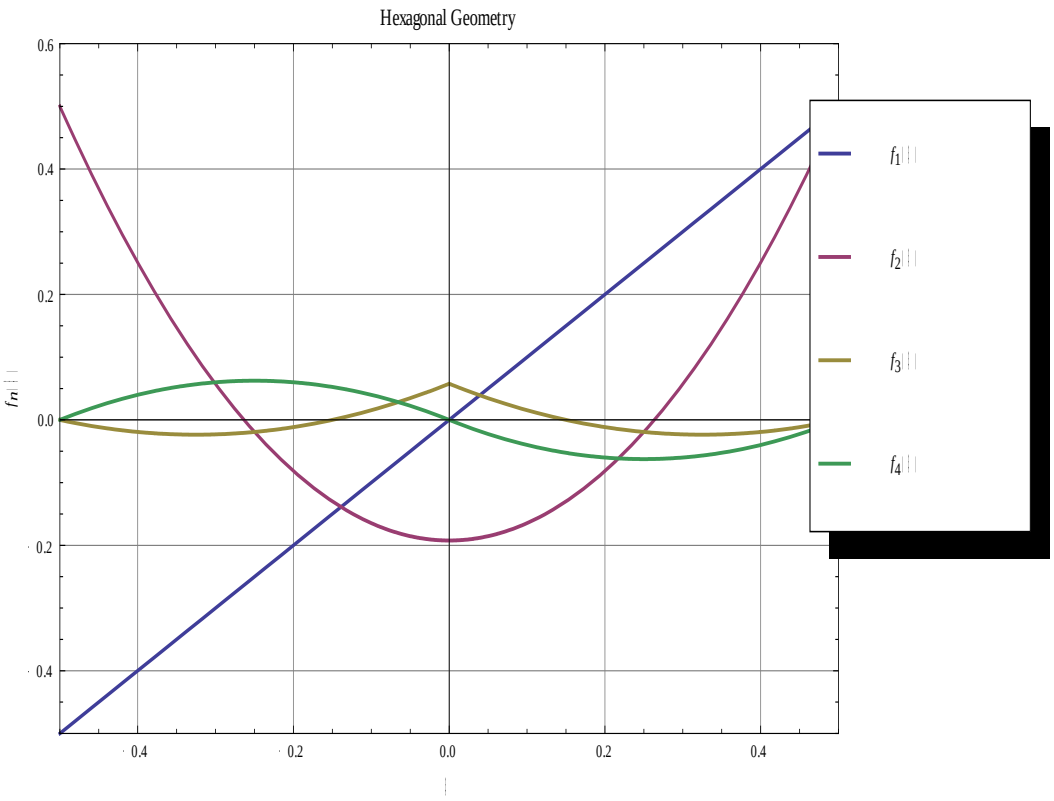

Figure 3.7 Polynomial expansion functions in hexagonal geometry

3.1.3.6 Solution of the transverse-integrated equations in hexagonal geometry

The surface-averaged currents at the left x-directed surfaces of the hexagon are given by equations analogous to (3.35) and (3.36),

$$J_{gx+}^{out} = \left[\frac{1}{2y_s(x)}\int_{-y_s(x)}^{y_s(x)} dy\left(-\frac{E_{gxx}}{\Sigma_{gt}}\Phi_g(x,y)\right)\right]_{x=\frac{h}{2}} - \frac{2\sqrt{3}}{h}\frac{E_{gxy}}{\Sigma_{gt}}\left[J_{gu}^{out}(h/2)+J_{gu}^{in}(h/2)-J_{gv}^{out}(h/2)-J_{gv}^{in}(h/2)\right]+J_{gx+}^{in} \tag{3.52}$$

In the following paragraphs we will describe the derivation of (3.52). We start from the expression for the net current in the x direction in the Q-D form, without including the energy group index g (all the quantities refer to neutrons within the same group).

$$J(x,y) = -\frac{E_{xx}}{\Sigma_t}\frac{\partial}{\partial x}\Phi(x,y) - \frac{E_{xy}}{\Sigma_t}\frac{\partial}{\partial y}\Phi(x,y) \tag{3.53}$$

In this case, the averaged net surface current is given by

$$\bar{J}_x\left(\frac{h}{2}\right) = \left[\frac{1}{2y_s(x)}\int_{-y_s(x)}^{y_s(x)} dy\left(\mathrm{J}_x(x,y)\right)\right]_{x=\frac{h}{2}}, y_s(x) = \frac{1}{\sqrt{3}}(h-|x|) \tag{3.54}$$

Combining (3.53) and (3.54), the averaged net surface current results in

$$\bar{J}_x(\frac{h}{2}) = \left[\frac{1}{2y_s(x)} \int_{-y_s(x)}^{y_s(x)} dy(-\frac{E_{xx}}{\Sigma_t}\frac{\partial}{\partial x}\Phi(x,y) - \frac{E_{xy}}{\Sigma_t}\frac{\partial}{\partial y}\Phi(x,y)) \right]_{x=\frac{h}{2}} \tag{3.55}$$

The first term of the integrand in (3.55) is the surface-averaged diffusive component of the net current across the surface at *h/2*,

$$\bar{J}_x^D(\frac{h}{2}) = \left[\frac{1}{2y_s(x)} \int_{-y_s(x)}^{y_s(x)} dy(-\frac{E_{xx}}{\Sigma_t}\frac{\partial}{\partial x}\Phi(x,y)) \right]_{x=\frac{h}{2}} \tag{3.56}$$

and the second term is the Q-D component of the net current across the surface at *h/2*

$$\bar{J}_x^Q(\frac{h}{2}) = \left[\frac{1}{2y_s(x)} \int_{-y_s(x)}^{y_s(x)} dy(-\frac{E_{xy}}{\Sigma_t}\frac{\partial}{\partial y}\Phi(x,y)) \right]_{x=\frac{h}{2}} \tag{3.57}$$

The Q-D component of the net current across the surface at *h/2* (3.57) can be further manipulated as in (3.58)

$$\begin{aligned} \bar{J}_x^Q(\frac{h}{2}) &= \left[\frac{1}{2y_s(x)} \int_{-y_s(x)}^{y_s(x)} dy(-\frac{E_{xy}}{\Sigma_t}\frac{\partial}{\partial y}\Phi(x,y)) \right]_{x=\frac{h}{2}} \\ &= \left[\frac{1}{2y_s(x)} \int_{-y_s(x)}^{y_s(x)} dy(-\frac{E_{xy}}{\Sigma_t})(\Phi(x,y_s(x)) - \Phi(x,-y_s(x))) \right]_{x=\frac{h}{2}} \\ &\cong -(\frac{\sqrt{3}}{h}\frac{E_{xy}}{\Sigma_t})(\bar{\Phi}_u(\frac{h}{2}) - \bar{\Phi}_v(-\frac{h}{2})) \end{aligned} \tag{3.58}$$

In the derivation of (3.58) we used that

$$\left[\frac{1}{2y_s(x)}\right]_{x=\frac{h}{2}} = \frac{\sqrt{3}}{h},$$
$$\left[\Phi(x, y_s(x))\right]_{x=\frac{h}{2}} \cong \bar{\Phi}_u(h/2), \tag{3.59}$$
$$\left[\Phi(x, -y_s(x))\right]_{x=\frac{h}{2}} \cong \bar{\Phi}_v(-h/2)$$

with the axes *u* and *v* as shown in Figure 3.2.

As shown in (Law, 1983), the surface-averaged fluxes $\bar{\Phi}_u(\frac{h}{2})$ and $\bar{\Phi}_v(-\frac{h}{2})$ can be represented in terms of incoming and outgoing surface-averaged currents $J_u^{in}(\frac{h}{2})$, $J_u^{out}(\frac{h}{2})$, $J_v^{in}(-\frac{h}{2})$, and $J_v^{out}(-\frac{h}{2})$:

$$\bar{\Phi}_u(\frac{h}{2}) = 2[J_u^{in}(\frac{h}{2}) + J_u^{out}(-\frac{h}{2})]$$
$$\bar{\Phi}_v(-\frac{h}{2}) = 2[J_v^{in}(-\frac{h}{2}) + J_v^{out}(-\frac{h}{2})] \tag{3.60}$$

Based on equations (3.55) to (3.60), the response matrix (Law, 1983) is then

$$J_{gx+}^{out} = \left[\frac{1}{2y_s(x)}\int_{-y_s(x)}^{y_s(x)} dy(-\frac{E_{gxx}}{\Sigma_{gt}}\Phi_g(x,y))\right]_{x=\frac{h}{2}} - \frac{2\sqrt{3}}{h}\frac{E_{gxy}}{\Sigma_{gt}}\left[J_{gu}^{out}(h/2) + J_{gu}^{in}(h/2) - J_{gv}^{out}(h/2) - J_{gv}^{in}(h/2)\right] + J_{gx+}^{in} \tag{3.61}$$

identical to (3.52). The first term, as we mentioned before, is the diffusive component of the current and can be further approximated with a multidimensional polynomial expansion such as the one in (3.51). The next step is to determine the coefficients of this expansion, a_{gxn}, n=1 to 4.

Expansion coefficients a_{gx1} and a_{gx2} depend upon fluxes as shown in equations (3.21) and (3.22). Basis function $f_3(x)$ has a first derivative discontinuity at *x=0*. Coefficient a_{gx3} is calculated by requiring that the semi-transverse integrated flux given by equation (3.44) is consistent with the discontinuity condition shown by its first derivatives at *x=0*. The expansion coefficient a_{gx4} is calculated by the method of weighted residuals, similar to the method described for Cartesian geometry, with the difference that we use the sign function *sgn(x)* as weight function (Law,1983):

$$w_1(x) \equiv y'(x) = -\frac{1}{\sqrt{3}}\mathrm{sgn}(x),$$
$$\mathrm{sgn}(x) = \begin{cases} -1, x \prec 0 \\ 0, x = 0 \\ +1, x \succ 0 \end{cases}. \tag{3.62}$$

Equations analogous to (3.46) apply to partial surface-averaged currents on the *u*- and *v*- directions of the node. The method briefly described here, applied on the *x*-, *u*-, and *v*-directions, preserves neutron balance. Computation of high-order expansion coefficients is laborious, and is described in detail in (Law, 1983).

For illustration purpose we present in (3.63) to (3.67) the Mathematica-generated equations used to build the matrix problem in hexagonal geometry. Equation (3.63) and (3.64) are the neutron balance equations in the fast and thermal group, (3.65) and (3.66) are the fast and thermal first-order moments of the one-dimensional balance equation, and equation (3.67) shows the response matrix equations, respectively. In the latter we skipped the group index *g*, the equations having the same form for both neutron groups:

$$\begin{aligned}&\frac{2}{3h}(-J_{u1}^{in}(-h/2)-J_{u1}^{in}(h/2)+J_{u1}^{out}(-h/2)+J_{u1}^{out}(h/2)-\\&J_{v1}^{in}(-h/2)-J_{v1}^{in}(h/2)+J_{v1}^{out}(-h/2)+J_{v1}^{out}(h/2))+\\&\frac{2}{3h}(-J_{x1}^{in}(-h/2)-J_{x1}^{in}(h/2)+J_{x1}^{out}(-h/2)+J_{x1}^{out}(h/2))+\overline{\Phi_1}\Sigma_{r1}=\\&\frac{\nu\Sigma_{f1}\overline{\Phi_1}+\nu\Sigma_{f2}\overline{\Phi_2}}{k}\end{aligned} \qquad (3.63)$$

$$\frac{2}{3h}(-J_{u2}^{in}(-h/2)-J_{u2}^{in}(h/2)+J_{u2}^{out}(-h/2)+J_{u2}^{out}(h/2)-$$
$$J_{v2}^{in}(-h/2)-J_{v2}^{in}(h/2)+J_{v2}^{out}(-h/2)+J_{v2}^{out}(h/2))+ \quad (3.64)$$
$$\frac{2}{3h}(-J_{x2}^{in}(-h/2)-J_{x2}^{in}(h/2)+J_{x2}^{out}(-h/2)+J_{x2}^{out}(h/2))-$$
$$\overline{\Phi_1}\Sigma_{12}\overline{+\Phi_2}\Sigma_{r2}=0$$

$$\frac{2}{3h}(J_{u1}^{in}(-h/2)-J_{u1}^{in}(h/2)-J_{u1}^{out}(-h/2)+J_{u1}^{out}(h/2))-$$
$$\frac{2}{3h}(J_{v1}^{in}(-h/2)-J_{v1}^{in}(h/2)-J_{v1}^{out}(-h/2)+J_{v1}^{out}(h/2))+ \quad (3.65)$$
$$\frac{2}{3h}(J_{x1}^{in}(-h/2)-J_{x1}^{in}(h/2)-J_{x1}^{out}(-h/2)+J_{x1}^{out}(h/2))+\Phi_{1x1}\Sigma_{r1}-$$
$$\frac{8E_{xx1}}{3h^2\Sigma_{t1}}(12\Phi_{1x1}+\frac{10}{3}(J_{x1}^{in}(-h/2)-J_{x1}^{in}(h/2)+J_{x1}^{out}(-h/2)+J_{x1}^{out}(h/2)))=$$
$$\frac{\nu\Sigma_{f1}\Phi_{1x1}+\nu\Sigma_{f2}\Phi_{2x1}}{k}$$

$$\frac{2}{3h}(J_{u2}^{in}(-h/2)-J_{u2}^{in}(h/2)-J_{u2}^{out}(-h/2)+J_{u2}^{out}(h/2))-$$
$$\frac{2}{3h}(J_{v2}^{in}(-h/2)-J_{v2}^{in}(h/2)-J_{v2}^{out}(-h/2)+J_{v2}^{out}(h/2))+ \quad (3.66)$$
$$\frac{2}{3h}(J_{x2}^{in}(-h/2)-J_{x2}^{in}(h/2)-J_{x2}^{out}(-h/2)+J_{x2}^{out}(h/2))-\Phi_{1x1}\Sigma_{12}-$$
$$\frac{8E_{xx2}}{3h^2\Sigma_{t2}}(-12\Phi_{2x1}+\frac{10}{3}(J_{x2}^{in}(-h/2)-J_{x2}^{in}(h/2)+J_{x2}^{out}(-h/2)+J_{x2}^{out}(h/2)))+$$
$$\Sigma_{r2}\Phi_{2x1}=0$$

$$\frac{6}{133}(J_u^{in}(-h/2)-J_u^{out}(-h/2)+J_v^{in}(h/2)-J_v^{out}(h/2))+$$
$$\frac{13}{133}(J_u^{in}(h/2)-J_u^{out}(-h/2)+J_v^{in}(-h/2)-J_v^{out}(-h/2))-$$
$$J_x^{in}(h/2)(1-\frac{4936}{399}\frac{E_{xx}}{h\Sigma_t})+J_x^{out}(h/2)(1+\frac{4936}{399}\frac{E_{xx}}{h\Sigma_t})-12\frac{E_{xx}\Phi_{1x}}{h\Sigma_t}-\frac{36}{7}\frac{E_{xx}\bar{\Phi}}{h\Sigma_t}- \quad (3.67)$$
$$\frac{832}{399}\frac{E_{xx}J_x^{in}(-h/2)}{h\Sigma_t}-\frac{832}{399}\frac{E_{xx}J_x^{out}(-h/2)}{h\Sigma_t}-$$
$$2\sqrt{3}\frac{E_{xy}}{h\Sigma_t}(J_u^{in}(h/2)+J_u^{out}(h/2)-J_v^{in}(-h/2)-J_v^{out}(-h/2))=0$$

In (3.65) and (3.66) the quantities Φ_{1x1} and Φ_{1x2} are the first moments of the fast flux and thermal flux, respectively; since (3.67) is basically the same for both groups and we did not include the group index, Φ_{1x} simply stands for the first moment of the flux.

3.1.3.7 Quasi-diffusion functionals (Eddington tensor)

To calculate the quasi-diffusion coefficients, also known as Eddington tensor elements or Eddington functionals, we use the spherical harmonics expansion of the neutron angular flux

$$\psi(\hat{r},\Omega)=\sum_{l=0}^{\infty}\sum_{m=-l}^{l}\Phi_l^m(\hat{r})Y_{lm}^*(\Omega) \quad (3.68)$$

and the definition of the Eddington functionals

$$E_{ij}(\hat{r})=\frac{\int_{4\pi}\Omega_i\Omega_j\psi(\hat{r},\hat{\Omega})d\hat{\Omega}}{\int_{4\pi}\psi(\hat{r},\hat{\Omega})d\hat{\Omega}} \qquad \text{i,j=x,y,z} \quad (3.69)$$

Combining the two equations leads to

$$E_{ij}(\hat{r}) = \frac{\sum_{l=0}^{\infty}\sum_{m=-l}^{l}\Phi_l^m(\hat{r})\int_{4\pi}\Omega_i\Omega_j Y_{lm}^*(\hat{\Omega})d\hat{\Omega}}{\sum_{l=0}^{\infty}\sum_{m=-l}^{l}\Phi_l^m(\hat{r})\int_{4\pi}Y_{lm}^*(\Omega)d\hat{\Omega}} \tag{3.70}$$

From the definitions above, the Eddington functionals are linear combinations of the moments of the angular flux $\Phi_l^m(\hat{r})$. The denominator of the last equation is the (scalar) neutron flux $\Phi_0^0(\hat{r})$. The coefficients of the expansion are given by the integrals over solid angle.

In the methodology used by Attila, even and odd-parity spherical harmonics are used. Table 3.1 shows even and odd harmonics and indicates in which of the Eddington functionals E_{ij} they are being used in Attila.

Table 3.1 Spherical harmonics used in Attila transport calculations

Parity	**Spherical harmonic**	***ij***
even	$Y_l^m(\Omega) = \sqrt{C_l^m}P_l^m(\mu)\cos(m\omega)$	*xx, yy, zz*
odd	$Y_l^m(\Omega) = \sqrt{C_l^m}P_l^m(\mu)\sin(m\omega)$	*xy, xz, yz*

In the expressions of the spherical harmonics

$$C_l^m = (2-\delta_{m0})(2l+1)(l-m)!/(l+m)! \tag{3.71}$$

where δ_{mo} is the Kronecker symbol, and $P_l^m(\mu)$ are the associated Legendre functions (Lew1993).

Assuming polar x-axis, truncating the expansion to a maximum order *l*=2, the orders *(l,m)* of the spherical harmonics used for each Eddington functional are summarized in Table 3.2.

Table 3.2 Angular flux moments used to calculate the Eddington tensor components

Functional	*l*	*m*
E_{xx}	*0* *2* *2*	*0* *0* *2*
E_{xy}	*2*	*-1*
E_{xz}	*2*	*-1*
E_{yy}	*0* *2* *2*	*0* *0* *2*
E_{yz}	*2*	*-2*
E_{zz}	*0* *2* *2*	*0* *0* *2*

Table 3.3 shows a brief list of associated Legendre functions, *l=0,1,* and *2* and corresponding coefficients C_l^m.

Table 3.3 Associated Legendre functions, l=0,1, and 2 and corresponding coefficients C_l^m

l	m	$P_l^m(\mu)$	C_l^m
0	0	1	1
1	0	μ	$\sqrt{3}$
1	1	$-\sqrt{(1-\mu^2)}$	$\sqrt{3}$
2	0	$(3\mu^2-1)/2$	$\sqrt{5}$
2	1	$-3\mu\sqrt{(1-\mu^2)}$	$\sqrt{(5/3)}$
2	2	$3(1-\mu^2)$	$\sqrt{(5/12)}$

The projections of the solid angle, Ω_x, Ω_y, and Ω_z, and the solid angle element $d\Omega$ are given by

$$\Omega_x = \mu$$
$$\Omega_y = \sqrt{(1-\mu^2)}\cos(\omega) \qquad (3.72)$$
$$\Omega_y = \sqrt{(1-\mu^2)}\sin(\omega)$$

$d\Omega = d\,\omega\, d\,\mu,\quad -1 \le \mu \le +1 \text{ and } 0 \le \mu \le 2\pi$

Performing the integrals over the solid angle gives the following expressions for the Eddington tensor elements (for simplicity, we will omit the dependence of position in the expression of the moments of the neutron flux). One should notice in particular that the integrals corresponding to *l=0, m=0* equal *1/3.* This is the diffusion approximation, when all off-diagonal components of the Eddington tensor cancel.

In Table 3.4 we summarize the results of the integration over solid angle.

Table 3.4 Integrals over the solid angle used in computing Eddington functionals

Functional	**l**	**m**	**Integral over dΩ**
E_{xx}	0	0	1/3
E_{xx}	2	0	2(√5)/15
E_{xx}	2	2	0
E_{xy}	2	-1	1/√15
E_{xz}	2	-1	1/√15
E_{yy}	0	0	1/3
E_{yy}	2	0	-(√5)/15
E_{yy}	2	2	1/√15
E_{yz}	2	-2	1/√15
E_{zz}	0	0	1/3
E_{zz}	2	0	-(√5)/15
E_{zz}	2	2	-1/√15

Assuming polar x-axis, the projections of the solid angle $\hat{\Omega}$ are as indicated in Equations 3.52. Truncating the expansion to a maximum order l=2, and performing the integrals over the solid angle demonstrates that the expressions of the Eddington functionals in terms of moments of the angular flux are (for simplicity, we will omit the dependence of position):

$$
\begin{aligned}
E_{xx} &= \frac{1}{3} + \frac{2\sqrt{5}}{15}\frac{\Phi_2^0}{\Phi_0^0} \\
E_{xy} &= \frac{1}{\sqrt{15}}\frac{\Phi_2^1}{\Phi_0^0} \\
E_{xz} &= \frac{1}{\sqrt{15}}\frac{\Phi_2^{-1}}{\Phi_0^0} \\
E_{yy} &= \frac{1}{3} - \frac{\sqrt{5}}{15}\frac{\Phi_2^0}{\Phi_0^0} + \frac{1}{\sqrt{15}}\frac{\Phi_2^2}{\Phi_0^0} \\
E_{yz} &= \frac{1}{\sqrt{15}}\frac{\Phi_2^{-2}}{\Phi_0^0} \\
E_{zz} &= \frac{1}{3} - \frac{\sqrt{5}}{15}\frac{\Phi_2^0}{\Phi_0^0} - \frac{1}{\sqrt{15}}\frac{\Phi_2^2}{\Phi_0^0}
\end{aligned}
\tag{3.73}
$$

In order to obtain the Eddington functionals in the system of hexagonal coordinates *x*-*u*-*v* and use them in Mathematica calculations we apply coordinate transformations to the functionals in the plane *x*-*z* containing the hexagonal cross-sections of the fuel assemblies in the Attila solid geometry model,

$$
E' = TET^{-1} \tag{3.74}
$$

where E' is the Eddington tensor (E_{nm}) in Mathematica orthogonal coordinates *x-x'*, *u-u'*, or *v-v'* , T and T^{-1} are the rotation matrix and its inverse, and E is the Eddington tensor in the system of Cartesian coordinates in the *x-z* plane of the Attila solid geometry model:

$$E' = \begin{pmatrix} E_{nn} & E_{nm} \\ E_{nm} & E_{mm} \end{pmatrix}$$
$$E = \begin{pmatrix} E_{xx} & E_{xz} \\ E_{xz} & E_{zz} \end{pmatrix} \qquad (3.57)$$
$$T = \begin{pmatrix} \cos\theta & \sin\theta \\ -\sin\theta & \cos\theta \end{pmatrix}$$

For transformations to *x-x'*, *u-u'*, and *v-v'* the angle θ is -30°, +30°, and +90°, respectively.

To calculate average Eddington tensor components E_{ij} over the regions *r* of the discretized Attila solid model we first had to calculate cell-averaged and region-averaged moments of the angular flux, $\left\langle \Phi_l^m \right\rangle_{c,r}$

$$\left\langle \Phi_l^m \right\rangle_c = \frac{1}{4}\sum_{k=1}^{4}\left(\Phi_l^m\right)_k$$
$$\left\langle \Phi_l^m \right\rangle_r = \frac{\sum_{c\in r}\left\langle \Phi_l^m \right\rangle_c V_c}{\sum_{c\in r} V_c} \qquad (3.76)$$

where $\left(\Phi_l^m\right)_k, k = \overline{1,4,}$ are the four *(l,m)* moments of the angular flux in the vertices of each of the tetrahedral cells *c* which comprise region *r*. The volume V_c of a tetrahedral cell is calculated knowing the position vectors $\vec{a}$, $\vec{b}$, $\vec{c}$, and $\vec{d}$ of its vertices (nodes)

$$V_c = \frac{1}{6}\left|(\vec{a}-\vec{d})\bullet((\vec{b}-\vec{d})\times(\vec{c}-\vec{d}))\right| \tag{3.77}$$

The coordinates *x, y, z* of the nodes and the cells that belong to each region are written in the mesh log file generated by Attila.

3.1.3.8 Validation of the solution strategies (diffusion case)

The implementation of this methodology was tested on a set of few-node, constant cross-section, Cartesian and hexagonal-mesh diffusion problems and the results were compared to literature (Pal 1997), (Heb, 2007). The test problem calculations were performed by using a program in Mathematica®, which provided the node-averaged flux and the k-eigenvalue calculated by the power iteration technique (Rad 1992). The results of the few-node diffusion problems are presented in the Sections 3.1.3.8.1 and 3.1.3.8.2 of this dissertation.

3.1.3.8.1 Multiple-node UO-MOX problems in Cartesian geometry

In the multiple-node problems the k-eigenvalues and the assembly powers are calculated, without the use of discontinuity factors, for the configurations shown in Fig. 3.8. Here, UX, PX, and R stand for UO_2, MOX, and water, respectively.

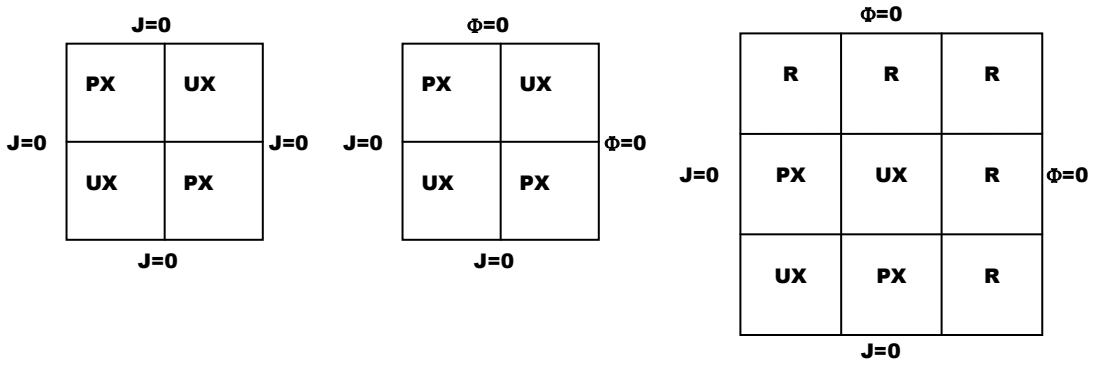

(C1) **(C2)** **(C3)**

Figure 3.8 UO2-MOX (C1, C2) and UO2-MOX-water (C3) configurations

The cross-sections for these problems were generated from single assembly, zero-current boundary conditions, Nuclear Energy Agency Committee on Reactor Physics (NEACRP) benchmark calculations (Pal 1997) and are presented in Table 3.5. As usual, the indices 1 and 2 refer to fast and thermal groups, respectively.

Table 3.5 Assembly homogenization results for NEACRP benchmark

Homogenized parameter	Assembly type		
	UX	PX	UA
$k_{\inf}$	0.998181	1.026669	0.660288
Σ_{t1}	0.277778	0.277778	0.277778
Σ_{t2}	0.833333	0.833333	0.833333
Σ_{a1}	0.009226	0.013791	0.012392
Σ_{a2}	0.092663	0.231691	0.138618
$\upsilon\Sigma_{f1}$	0.004570	0.006852	0.004580
$\upsilon\Sigma_{f2}$	0.113537	0.344583	0.117526
Σ_{21}	0.020430	0.015864	0.019209

The results of the calculations are presented in Table 3.6, together with the relative errors. One set of calculations was performed assuming flat leakage, and another set assuming quadratic leakage. The reference solutions were obtained by 2-D, 2-group, heterogeneous static diffusion calculations, with one node per fuel pin (Pal 1997) and are shown in Table 3.7.

Table 3.6 NEACRP benchmark, homogenized node calculations

Confi-guration	Flat Leakage Approximation				Quadratic Leakage Approximation			
	k-eff	Error %	Power UX/MOX	Error %	k-eff	Error %	Power UX/MOX	Error %
C1	1.01846	-0.07	0.7865	1.2	1.01863	-0.05	0.7937	2.1
C2	0.91112	0.47	1.0671	0.86	0.90638	-0.05	1.0710	1.2
C3	0.93772	-0.04	0.8718	3.1	0.93565	-0.26	0.8779	3.8

Table 3.7 NEACRP benchmark, homogenized node calculations, reference values (Pal 1997)

Configuration	Reference Values	
	k-eff	Power UX/MOX
C1	1.01914	0.7773
C2	0.90685	1.058
C3	0.93806	0.8459

3.1.3.8.2 Multiple node problems in hexagonal geometry

The IAEA 2-D benchmark reactor (Heb, 2007), a 20 hexagonal node problem is used to demonstrate the implementation, in hexagonal geometry, of the method proposed here. The layout is illustrated in Figure 3.9.

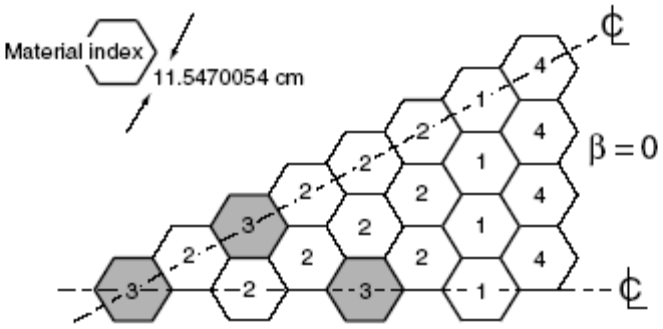

Figure 3.9 The hexagonal IAEA 2-D reactor.

The benchmark consists of 13 rodded assemblies, mixtures 1 and 2, three assemblies with high absorption for thermal neutrons, mixture 3, and four assemblies filled with moderator, mixture 4, in a 30 degree symmetry. The reference k_{eff} is 1.005512 (Heb, 2007). The cross-section data for the IAEA 2-D benchmark are shown in Table 3.8.

Table 3.8 Cross-section data for IAEA 2-D benchmark (Heb, 2007)

Mixture	Group	D^g (cm)	Σ_r^g (cm^{-1})	$\nu\Sigma_f^g$ (cm^{-1})	$\Sigma_{s0}^{g\to g+1}$ (cm^{-1})
1	1	1.5	3.0×10^{-2}	0.0	2.0×10^{-2}
	2	0.4	8.0×10^{-2}	1.35×10^{-1}	
2	1	1.5	3.0×10^{-2}	0.0	2.0×10^{-2}
	2	0.4	8.5×10^{-2}	1.35×10^{-1}	
3	1	1.5	3.0×10^{-2}	0.0	2.0×10^{-2}
	2	0.4	1.3×10^{-1}	1.35×10^{-1}	
4	1	1.5	4.0×10^{-2}	0.0	4.0×10^{-2}
	2	0.4	1.0×10^{-2}	0.0	

The methodology described in Section 3.1.3 implemented in a program in Mathematica, was used to calculate the multiplication factor (k_{eff}) and the node power. Calculations were performed with the diffusion approximation and assuming flux and

current continuity, and resulted in a k_{eff} equal to 1.00100 (0.45 % less than the reference value).

The k-eigenvalue and power distribution diffusion calculations performed to validate the transverse-integration methodology have provided results in fair agreement with the benchmark results. The discrepancies shown especially in the case of multiple-node, unlike-neighbor problems are comparable to those reported by other authors (Pal 1997). We expect to improve the agreement with the reference cases by using the QD methodology.

Limitations in the accuracy are also due to the approximation of constant-QD functionals across the fuel assemblies and the quality of the single-assembly homogenized cross-sections.

3.1.3.9 Validation of the solution strategies (quasi-diffusion case)

The results of the quasi-diffusion, Mathematica, code are validated against calculations performed using Attila particle transport code (McGhee 2009). Attila is a three-dimensional, arbitrary-order anisotropic scattering, multi-group energy discretization, S_N particle transport code. Both upscatter and downscatter are allowed; however, because of the cut-off energy of the neutrons in the fast group (0.625 eV) and the elemental composition of the media in this research no upscatter is physically present. Due to Attila's flexibility, several user options are currently available, such as cross-section energy group collapse, vacuum/reflecting boundary conditions, and transport solver options (maximum scattering degree, S_N order, quadrature set, convergence

criteria). Attila allows the user to set material composition (atom fractions or mass fractions) and attribute materials to various regions of the solid model.

The elemental compositions, in atom fractions, of the materials used in the benchmarking calculations are presented in Table 3.9.

Table 3.9 Isotopic composition of the Attila regions

Isotope	**Fuel U (4.0 g/cm^3)**	**Fuel Pu(4.0 g/cm^3)**	**Gas Annulus (1.8×10^{-3}g/cm^3)**
B-10	1.21373×10^{-7}	1.21373×10^{-7}	0
B-11	1.43230×10^{-7}	1.43230×10^{-7}	0
C-12	9.95154×10^{-1}	9.95154×10^{-1}	3.33333×10^{-1}
O-16	6.73646×10^{-4}	6.73646×10^{-4}	6.66667×10^{-1}
Si-28	3.75891×10^{-3}	3.75891×10^{-3}	0
U-235	4.25274×10^{-5}	0	0
U-238	3.70682×10^{-4}	3.70682×10^{-4}	0
Pu-239	0	4.25274×10^{-5}	0

Attila's multi-group energy discretization also allows collapsing multi-group cross-sections to a small number of groups (few-group). In the present cases, 22-group neutron cross-sections were collapsed to two-group cross-sections: fast-group neutrons between 20 MeV and 0.625 eV, and thermal neutrons of energies below the 0.625 eV threshold. For the given isotopic compositions, no upscattering is present. The fission neutron spectrum was assumed to be the mixed spectrum of the two main fissile isotopes present in the mixtures, U-235 and Pu-239.

Attila binary restart files provide information on neutron flux moments up to the maximum scattering order set by the user, the neutron currents through the faces of the tetrahedra, and the neutron scalar fluxes averaged over the faces of the tetrahedra Flux moments given by the restart file are the values at the vertices of the tetrahedra that form

the Attila computational grid. Scalar fluxes and currents are, in addition, given as average values over the sides of the tetrahedral cells. A maximum scattering order of two leads to nine moments (Table 3.10):

Table 3.10 The first two scattering moments (l,m)

l	***m***
0	*0*
1	*-1,0,1*
2	*-2,-1,0,-1,2*

The quasi-diffusion (Eddington) functionals can be derived in terms of the moments of the neutron flux, as shown in (3.58). The moments of the neutron flux are extracted from the binary Attila restart files.

Current cross-section libraries available in Attila and used in this research are the *transpire29* cross-section libraries. They apply to 22 neutron energy groups and seven gamma energy groups. Only the 22 neutron energy groups were used in the calculations presented here. The maximum scattering order in these libraries is three (P_3). In order to be consistent with the quasi-diffusion functionals that depend on just the flux moments of maximum scattering order of two, the Attila cross-section libraries corresponding to the isotopes which comprise the Attila regions of the problems presented here (B-10, B-11, C-12, O-16, Si-28, U-235, U-238, and Pu-239) were manually post-processed and truncated to a maximum scattering order of two (P_2). Due to the flexibility of the Attila transport solver, the user is allowed to choose the scattering treatment; for the P_2 case, the Galerkin scattering treatment is recommended (McGhee 2009).

The three-dimensional geometry models Attila uses to generate the computational grid are based on CAD SolidWorks, Parasolid, models (OSU COE). After the Parasolid

model was generated, it is saved as a solid model in an Attila file with the extension *x_t*. Subsequently, Attila generates the computational grid, available to user in the form of an *ascii-rtt* file. The *rtt* file caries information on: maximum size and shape of the cells in the grid, number of nodes (vertices), vertex coordinates, sides, and cells (neighboring cells and the Attila region to which a cell belongs).

The Eddington tensor components E_{ij} over the regions *r* of the discretized Attila solid model are calculated using equations (3.51), based on cell-averaged and region-averaged moments of the angular flux, $\left\langle \Phi_l^m \right\rangle_{c,r}$

where $\left(\Phi_l^m\right)_k, k=\overline{1,4,}$ are the four *(l,m)* moments of the angular flux in the vertices of each of the tetrahedral cells *c* comprising region *r*. Alternatively, cell-averaged scalar fluxes can be calculated by using the values of the flux on the faces of the tetrahedral cell given in the Attila restart file. The volume V_c of a tetrahedral cell is calculated knowing the position vectors (coordinates) $\vec{a}$, $\vec{b}$, $\vec{c}$, and $\vec{d}$ of its vertices (nodes), as shown in (3.62). The Eddington tensor components and cell-averaged scalar fluxes are calculated using specialized programs written in Mathematica.

3.1.3.10 The power method for finding the highest value eigenvalue

The multiplication factor *k* of a system containing fissionable material depends on the ratio between the rate at which neutrons are generated by fission and the rate at which neutrons are absorbed in the system or leave the system due to leakage. The

multiplication factor is the highest value eigenvalue of the matrix problem equivalent to the systems of equations described in this section for Cartesian and hexagonal geometry.

The equivalent matrix formulation of the QD eigenvalue problem is

$$M\nu = \frac{1}{k} F\nu \tag{3.78}$$

where *M* is the square matrix of the source-free system and *F* is the square matrix of fission sources, and *k* is the multiplication factor.

This problem is equivalent to this standard form of the eigenvalue problem

$$A\nu = k\nu \tag{3.79}$$

where $A = M^{-1}F$.

To find the value of the square matrix A, it is recommended (Rad 1992) to use the iterative numeric procedure known as the “power iteration” .

The iterative process starts with an almost arbitrarily-chosen column vector $\nu^{(1)}$. After a number *n* of iterations, the vector $u^{(n+1)}$

$$u^{(n+1)} = \frac{A\nu^{(n)}}{|A\nu^{(n)}|}, n \geq 1 \tag{3.80}$$

can be used to approximate the greatest eigenvalue *k*,

$$k^{(n)} = |A\nu^{(n)}| \tag{3.81}$$

where $|A\nu^{(n)}|$ is the norm of vector $A\nu^{(n)}$. The normalization by dividing to $|A\nu^{(n)}|$ is necessary to prevent too high or too low values for $u^{(n)}$.

3.1.3.11 Analytic derivation of the infinite-medium multiplication factor

Consider an infinite system or any equivalent non-leaking system. This simple derivation allows to analyze the balance between neutron production and neutron absorption in a system containing fissionable material.

The derivation starts with the balance equations for two neutron groups (fast *g=1*, and thermal *g=2*), where the symbols have the meanings shown in Section 3.1.1.

$$\begin{aligned}\nabla\bullet\hat{\mathrm{J}}_1(\hat{r})+\Sigma_{r1}(\hat{r})\Phi_1(\hat{r})&=\frac{1}{k}(\upsilon\Sigma_{f1}(\hat{r})\Phi_1(\hat{r})+\upsilon\Sigma_{f2}(\hat{r})\Phi_2(\hat{r}))\\ \nabla\bullet\hat{\mathrm{J}}_2(\hat{r})+\Sigma_{r2}(\hat{r})\Phi_2(\hat{r})&=\Sigma_{12}(\hat{r})\Phi_1(\hat{r})\end{aligned} \tag{3.82}$$

In infinite media, the leakage terms $\nabla\bullet\hat{\mathrm{J}}_1(\hat{r})$ and $\nabla\bullet\hat{\mathrm{J}}_2(\hat{r})$ are zero (Dud 1976), therefore equations (3.68) become

$$\begin{aligned}\Sigma_{r1}(\hat{r})\Phi_1(\hat{r})&=\frac{1}{k}(\upsilon\Sigma_{f1}(\hat{r})\Phi_1(\hat{r})+\upsilon\Sigma_{f2}(\hat{r})\Phi_2(\hat{r}))\\ \Sigma_{r2}(\hat{r})\Phi_2(\hat{r})&=\Sigma_{12}(\hat{r})\Phi_1(\hat{r})\end{aligned} \tag{3.83}$$

Solving for *k*, we find the value of the infinite medium multiplication factor k_∞

$$k_\infty=\frac{\upsilon\Sigma_{f1}}{\Sigma_{r1}}+\frac{\Sigma_{12}}{\Sigma_{r1}}\frac{\upsilon\Sigma_{f2}}{\Sigma_{r2}} \tag{3.84}$$

4 RESULTS

In this chapter we compare the results obtained solving the low-order QD equations with a code written in Mathematica for a series of problems with the results obtained by using the transport code Attila.

One-node and several-node three-dimensional (3-D) problems were simulated in Attila to test the quasi-diffusion algorithm in hexagonal geometry. In all cases the height (extent along the vertical y-axis in Attila solid model geometry) of the 3-D model is 20.0 cm, and the length of the side of the hexagon is 20.0 cm (flat-to-flat distance h=34.641 cm). Since the model implemented in Mathematica is a 2-D quasi-diffusion model, in the Attila 3-D model we chose reflecting surfaces at the top and bottom of the hexagonal fuel assemblies.

4.1 One Node Problems

One-node problems are a useful tool to check the accuracy of the diffusion/quasi-diffusion codes developed in Mathematica. They are also a useful test to evaluate the neutron cross-sections provided by output files of Attila.

In all cases the convergence criteria in the Mathematica quasi-diffusion code were chosen such that the relative variation of the neutron fluxes from one iteration to the next is less than 10^{-8}. Based on generally-accepted computational experience, the expected relative error in k_{eff} is, in this case, as low as 10^{-10}. Transport iterations of the Attila

calculations were chosen by the user to stop when the relative error in k_{eff} dropped below 10^{-6}.

4.1.1 Hexagonal prism

The model is a single homogeneous fuel assembly, uranium-type isotopic composition, as shown in Table 3.5. Vacuum boundary conditions apply in this case, since reflecting boundaries are allowed by Attila only for surfaces perpendicular to the Cartesian coordinate axes.

The macroscopic, two-group, neutron cross-sections extracted from the Attila material property output files for uranium-type fuel, are summarized in Table 4.1.

Table 4.1 Macroscopic cross-sections for uranium-type fuel region

Cross-section (cm^{-1})	**Fast neutrons ($g=1$)**	**Thermal neutrons ($g=2$)**
Transport Σ_{tr}	0.767947	0.959926
Removal Σ_r	0.009504	0.004700
Fission $\nu\Sigma_f$	0.000282701	0.00817226
Slowing-down Σ_{12}	0.00890329	n/a

The components of the Eddington tensor were calculated using the moments of the angular flux as provided in the Attila binary restart file, in Cartesian coordinates x-y-z. The components of the Eddington tensor in hexagonal coordinates were then derived using the properties of the tensor transforms. They are summarized in Table 4.2.

Table 4.2 The components of the Eddington tensor in hexagonal coordinates

Eddington tensor component	Fast neutrons (*g=1*)	Thermal neutrons (*g=2*)
E_{xx}	0.332926	0.333061
E_{uu}	0.332903	0.333064
E_{vv}	0.332882	0.333029
E_{xy}	0.0000119047	0.0000087119
E_{us}	-0.0000255863	-0.0000183607
E_{vw}	0.0000136816	0.00000864879

Although Attila does not allow reflecting (zero-current) boundary conditions on all the surfaces of the hexagonal geometry problem, the quasi-diffusion implementation in Mathematica does. Therefore, the Mathematica code was used to calculate the infinite-medium multiplication factor k_{inf} for the single-assembly hexagonal prism. This result was then compared to the k_{inf} of a square, reflected prism of the same composition, and to k_{inf} analytically calculated by using the cross-sections from the Attila material properties file.

4.1.2 Square prism

This problem assumes a single, homogeneous square prism, of uranium-type fuel (isotopic composition given in Table 3.5). This geometry presents the advantage that reflecting boundary conditions are allowed. Reflecting boundaries are allowed by Attila only for surfaces perpendicular to the Cartesian coordinate axes; due to their shape, hexagonal nodes cannot have reflecting boundary conditions. We calculated k_{inf} of the reflected square prism using Attila, Mathematica with Cartesian-geometry, and analytic, hand-calculations.

4.2 Four-Node Problems

Four-node problems consist of four assemblies, two disjoint assemblies with U-type fuel, and two adjacent assemblies with Pu-type fuel; isotopic compositions and densities are given in Table 4.3. Each assembly has a 3.5 cm-radius, gas-filled axial annulus. Transport cross-sections used in Mathematica calculations are the homogenized cross-sections of the U/Pu-type fuel rather than cross-sections homogenized over the whole assemblies-including the annulus. This approach better models neutron leakage at the boundaries of the fuel assemblies far from the central annuli.

A typical range of Eddington functionals for the four hexagonal node problem presented here is shown in Table 4.3 (values for the U-graphite and Pu-graphite regions, aka U/Pu "fuel"):

Table 4.3 Eddington functionals for the 4 hexagonal node problem

	E_{xx}		E_{uu}		E_{vv}	
	U	**Pu**	**U**	**Pu**	**U**	**Pu**
Fast	0.332027	0.333702	0.333952	0.332735	0.334029	0.332939
Thermal	0.330244	0.334311	0.334427	0.332721	0.334727	0.332518

Table 4.3 (cont'd) Eddington functionals for the 4 hexagonal node problem

	E_{xy}		E_{us}		E_{vw}	
	U	**Pu**	**U**	**Pu**	**U**	**Pu**
Fast	-4.47e-5	-1.181e-4	1.156e-3	-4.406e-4	-1.1111e-3	5.586e-4
Thermal	-1.73e-4	1.169e-4	2.588e-3	-1.1035e-3	9.179e-4	2.588e-3

4.3 Seven-Node Problems

Seven-node problems consist of seven assemblies, six with U-type fuel, around a central assembly with Pu-type fuel. Each assembly has a 3.5 cm-radius, gas-filled axial annulus.

Transport cross-sections used in Mathematica calculations are the homogenized cross-sections of the U/Pu -type fuel rather than cross-sections homogenized over the whole assemblies-including the annulus. This approach better models neutron leakage at the boundaries of the fuel assemblies far from the central annuli.

Attila calculations are summarized in the Table 4.4:

Table 4.4 Attila multiplication factors

Problem Description	$\underline{k}_{eff}/ki_{nf}$, Attila
Single assembly, homogeneous hexagonal prism, no annuli	0.4425224
Reflected square-base prism, same composition as uranium fuel (ki_{nf},)	1.6557332
Four hexagonal assemblies, 2 disjunct with U-type fuel, and 2 adjacent assemblies with Pu-type fuel, 3.5 cm-radius, gas-filled axial annuli in the center of each assembly.	1.11555
Seven hexagonal assemblies, 6 with U around a central assembly with Pu-type fuel, 3.5 cm-radius, gas-filled axial annuli in the center of each assembly.	1.3054192

Table 4.5 summarizes Mathematica-HEXQD effective multiplication factors in diffusion models, as well as in quasi-diffusion models. These results are compared to Attila model runs. Two infinite-medium problems, the reflected square-base prism and the single hexagonal assembly, no annuli, zero boundary currents show comparisons

between k_{inf} calculated using HEXQD, Attila, and analytic ("hand calculations"). The purpose of the k_{inf} calculations was to test the correct use of the cross-sections provided by Attila material properties file.

Table 4.5 Comparison between multiplication factors calculated using Attila, Mathematica quasi-diffusion code and analytic (hand calculations)

Problem Description	**k-eff, HEXQD, diffusion approximation**	**k-eff, Attila transport code**	**Error diffusion vs. Attila, in percent/pcm**	**k-eff, HEXQD, quasi-difussion approximation**	**Error HEXQD, quasi-diffusion diffusion vs. Attila, in percent/pcm**
Single assembly, homogeneous hexagonal prism, no annuli	0.487879	0.4425224	+10.2%/4536pcm	0.487879	+10.2%/4536pcm
Reflected square-base prism, same composition as uranium fuel (ki_{nf},)	1.658620	1.6557332	+0.17%/289pcm	n/a	n/a
Single assembly, no annuli, zero boundary currents (ki_{nf},- hand calculations)	1.658623	1.6557332	+0.17%/289pcm	n/a	n/a
Four hexagonal assemblies, 2 disjunct with U-type fuel, and 2 adjacent assemblies with Pu-type fuel, 3.5 cm-radius, gas-filled axial annuli in the center of each assembly.	1.09380	1.11555	-2.0 % /-2175 pcm	1.09362	-2.0%/-2193 pcm
Seven hexagonal assemblies, 6 with U around a central assembly with Pu fuel, 3.5 cm-radius, gas-filled axial annuli in the center of each assembly.	1.31316	1.3054192	+0.59% /774pcm	1.31319	0.60%/777pcm

5 DISCUSSION

As one could notice the effective multiplication factors with and without QD (i.e., pure diffusion) are very close. This is due to the fact that the 0-th moment of the angular flux is much bigger than the second order moments, therefore their ratio is much smaller than 1/3. This makes the diagonal Eddington functionals very close to 1/3, and the off-diagonal functionals are a few orders of magnitude smaller.

A typical range of Eddington functionals for the four hexagonal node problem (row 2, Table 4.5) presented here is shown in Table 4.3 (values for the U-graphite and Pu-graphite regions, aka U/Pu "fuel"). Eddington functionals in Table 4.3 were used in QD calculations for Problem 2, leading to k_{eff}=1.09362.

Fast and thermal flux moments for the same 4 hexagonal node problem is shown in Table 5.1. In Table 5.1, U1 and U2 stand for two fuel assemblies with U-235 and U-238, and Pu1 and Pu2 for assemblies with U-238 and Pu-239, respectively.

Table 5.1 Flux moments, uranium and plutonium fuel

Fast neutrons					
l	**m**	**U 1**	**U 2**	**Pu 1**	**Pu 2**
0	**0**	5.02319×10^{1}	4.73192×10^{1}	1.06466×10^{2}	1.04882×10^{2}
1	**-1**	2.50854×10^{0}	-2.16813×10^{0}	2.93429×10^{0}	-3.11681×10^{0}
1	**0**	1.4915×10^{0}	-1.8578×10^{0}	-3.91021×10^{0}	3.84948×10^{0}
1	**1**	-3.67329×10^{-4}	-3.72095×10^{-4}	-2.96916×10^{-4}	2.61914×10^{-3}
2	**-2**	-4.60056×10^{-5}	-2.09092×10^{-4}	-7.2691×10^{-4}	-5.11949×10^{-4}
2	**-1**	2.02739×10^{-1}	2.16285×10^{-1}	-2.5947×10^{-1}	-1.98225×10^{-1}
2	**0**	-1.19807×10^{-1}	-1.06338×10^{-1}	-1.3538×10^{-2}	-1.80452×10^{-5}
2	**1**	1.24149×10^{-4}	-2.64341×10^{-4}	-1.12492×10^{-3}	-1.73421×10^{-4}
2	**2**	-7.13236×10^{-2}	-6.12758×10^{-2}	1.69677×10^{-1}	1.61612×10^{-1}

Table 5.1(cont'd) Flux moments, uranium and plutonium fuel

Thermal neutrons					
l	**m**	**U 1**	**U 2**	**Pu 1**	**Pu 2**
0	**0**	5.02319×10^{1}	4.73192×10^{1}	1.06466×10^{2}	1.04882×10^{2}
1	**-1**	2.50854×10^{0}	-2.16813×10^{0}	2.93429×10^{0}	-3.11681×10^{0}
1	**0**	1.4915×10^{0}	-1.8578×10^{0}	-3.91021×10^{0}	3.84948×10^{0}
1	**1**	-3.67329×10^{-4}	-3.72095×10^{-4}	-2.96916×10^{-4}	2.61914×10^{-3}
2	**-2**	-4.60056×10^{-5}	-2.09092×10^{-4}	-7.2691×10^{-4}	-5.11949×10^{-4}
2	**-1**	2.02739×10^{-1}	2.16285×10^{-1}	-2.5947×10^{-1}	-1.98225×10^{-1}
2	**0**	-1.19807×10^{-1}	-1.06338×10^{-1}	-1.3538×10^{-2}	-1.80452×10^{-5}
2	**1**	1.24149×10^{-4}	-2.64341×10^{-4}	-1.12492×10^{-3}	-1.73421×10^{-4}
2	**2**	-7.13236×10^{-2}	-6.12758×10^{-2}	1.69677×10^{-1}	1.61612×10^{-1}

Scalar fluxes calculated by averaging the face fluxes of each tetrahedron in the corresponding Attila region (obviously fuel assemblies of the same composition and equivalent position have approximately the same scalar fluxes, as expected with the symmetry of the problem) - same 4 hexagonal node problem - can be used for cross-section homogenization, as shown in Table 5.2:

Table 5.2 Average fluxes over equivalent Attila regions (calculated using the four face fluxes of each tetrahedral cell)

Energy group	Attila region	Material	Scalar flux
Fast	4	Fuel Pu	108.591
	8	Fuel Pu	108.601
	2	Fuel U	48.8184
	6	Fuel U	48.8161
Thermal	4	Fuel Pu	77.2108
	8	Fuel Pu	77.2168
	2	Fuel U	54.1801
	6	Fuel U	54.1801

The use the average of the four values of the flux in the vertices of the tetrahedra leads moments as shown in Table 5.3:

Table 5.3 Average fluxes over equivalent Attila regions (calculated using flux values in the vertices of the tetrahedra)

Energy group	Attila region	Material	Scalar flux	Flux ratios,U1/U2,Pu1/Pu2
Fast	4	Fuel Pu1	106.466	1.015 (+1.5%)
	8	Fuel Pu2	104.882	
	2	Fuel U1	50.2319	1.062 (+6.2%)
	6	Fuel U2	47.3192	
Thermal	4	Fuel Pu1	75.3937	0.806 (-24%)
	8	Fuel Pu2	93.5960	
	2	Fuel U1	54.8606	0.834 (-20%)
	6	Fuel U2	65.772	

As the results presented here suggest, region-averaged fluxes based on tetrahedral cell-averaged fluxes calculated using face-averaged values seem to better agree with the symmetry of the problem, in the sense that it results in basically the same fluxes in the fuel assemblies of same composition and equivalent positions in the problem. The vertex-based calculations show discrepancies between 1.5% and -24%, the highest for thermal neutron fluxes (last column of Table 5.3).

The analysis of the results presented in Section 5 points out that the errors between Mathematica QD and Attila decrease with number of hexagonal nodes in zero-flux boundary condition problems.

The neutron currents across the inner and outer boundaries of the problems are determined by the diffusion constants of the materials in the immediate vicinity of the boundaries rather than by the node-homogenized constants, therefore the use of the fuel region transport cross-sections instead the annular assembly-homogenized transport cross-sections improves slightly the agreement between Mathematica and Attila.

The multiplication factor for infinite-medium (zero-current boundary conditions), homogeneous problems agree much better with Attila than those with zero flux boundary conditions, and confirm the correct use of fission, removal and slowing-down cross-sections from the Attila material properties output file.

The discrepancies between Attila and Mathematica can also be explained by the fact that Attila implicitly accounts for flux discontinuity at the borders of the assemblies, while the model implemented in Mathematica does not.

The effects of the QD are small and do not seriously affect the multiplication factor in neither of the geometries; however the effects are somewhat more important in Carthesian geometry compared to hexagonal geometry. One possible reason for this could be the higher number of coordinate axes in hexagonal geometry (three) compared to only two in Cartesian. This would reduce the influence of the neutrons streaming along one of the axes on the flow of neutrons on the other two directions. Another explanation could be nature of the main neutron- moderating species: carbon compared to hydrogen.

6 CONCLUSIONS AND FUTURE RESEARCH

The results summarized in Section 3.1 have been obtained for the particular case of diagonal components of value 1/3 and zero off-diagonal components of the Eddington tensor, i.e the diffusion approximation, and were used to verify the transverse-integrated equations implemented in the Mathematica quasi-diffusion code. The benchmarking was against published calculations, in Cartesian and hexagonal geometry, with author-provided cross-sections.

Unlike the results in Section 3.1, the one-node, four-node and seven-node problems presented in Section 4 required for benchmarking cross-sections and Eddington functionals were calculated using angular flux moments extracted from Attila material property and binary restart files. Apart from the transport cross-sections (and Eddington functionals), the Attila cross-sections as used in the Mathematica calculations satisfactorily compared to the analytic, infinite-medium, multiplication factor . Mathematica and Attila calculations show better agreement for the multiple-node problems, where the effect of the neutron leakage is less important (leakage rate is much smaller than absorption rate). This suggests that the leakage term accuracy can be improved.

The analysis of the moments of the angular neutron flux shows that the zero-order moment is much larger than the higher moments. The calculation of the Eddington functionals based on the moments of the angular neutron flux provided in the Attila binary restart files show clearly that the functionals do not significantly deviate from 1/3

so we can conclude that diffusion dominates the streaming of the neutrons, rather than the quasi-diffusion effects.

The use of the homogenized transport cross-section of the graphite-uranium (plutonium) regions rather than a homogenization that includes the gas annuli in the (quasi)diffusion term improves the results, since the leakage term is calculated at the boundaries of the fuel assemblies, far from the central annuli. Another good approach is to use, in calculating cell-averaged flux moments needed in evaluating the Eddington functionals, angular flux moments averaged over the faces of the tetrahedral rather than the moments in the vertices of the tetrahedral (both types of moments are available in the Attila restart files).

Future research may attempt to refine the computational grid (i.e., equilateral triangles instead full hexagons) and/or consider different sets of expansion functions. Investigations may also consider the change in results when the mesh consists of, for example, six triangles per hexagon and the expansion functions are quadratic or quartic polynomials. The decreased effect of quasi-diffusion in hexagonal geometry may be due to the increased number of coordinate axes in the hexagonal geometry (x-u-v) compared to Cartesian geometry (x-y), and this aspect may need to be addressed in future research. Another area of research may involve investigating the effect of isotopic compositions (homogenized cross-sections) on the magnitude of the quasi-diffusion effects.

7 REFERENCES

(Ada 1994) Adams, M.L., "Computational Methods for Particle Transport Problems-Course Notes" (1994)

(Ada 1994) Adams, M.L. and Larsen, E. W., "Fast Iterative Methods For Discrete Ordinates Particle transport Calculations", Progress in Nuclear Energy, Vol.40, No.1, pp3-159(2002)

(Aks 1979) Aksenov, N.N. and Gol'din, V. Ya., "Computation of the Two-Dimensional Stationary Equation of Neutron Transfer by the Quasi-Diffusion Method", USSR Comp. Math. and Math. Phys., v.19, pp263-266 (1979)

(Ame 1992) Ames, W. F., "Numerical Methods for Partial Differential Equations", Academic Press, Inc., New York (1992)

(Ani 1999) Anistratov, D. Y., Adams, M.L., Palmer, T. S., and Smith, K. S., " An Innovative Reactor Analysis Methodology Based on Quasidiffusion Nodal Core Model", DOE NERI Proposal (1999)

(Ani 2001) Anistratov, D. Y., Private Communication

(Ari 1993) Aristova, E. N. and Kolpakov, A. V., "A Combined Finite Difference Scheme for an Elliptic Operator in an Oblique-Angled Cell", *Math. Modeling Comp. Exp.* 1, 187 (1993)

(Cla 2002) Clarno, K. T. and Adams, M.L., "Improved Boundary Conditions for Assembly- Level Transport Codes", PHYSOR 2002, Seoul,Korea, October 7-10, 2002

(Cor 2006) www.core.org.cn

(Dud 1976) Duderstadt, J. J. and Hamilton, L. J., "Nuclear Reactor Analysis", John Wiley and Sons, Inc., New York (1976)

(Fer 2009) Ferrer, R.M., Ougoua, A.M., Bingham, A.A. "Nodal Green's Function Method Singular Source Term and Burnable Poison Treatment in Hexagonal Geometry", INL/EXT-09-16773, Idaho National Laboratory, Idaho Falls, ID, September, 2009.

(Gol 1967) Gol'din, V. Ya., " A Quasi-Diffusion Method of Solving the Kinetic Equation", USSR Comp. Math. and Math. Phys., v.4 (1967)

(Gol 1972) Gol'din, V. Ya. and Chetverushin, B. N., "Methods of Solving One-Dimensional Problems of Radiation Gas Dynamics", USSR Comp. Math. and Math. Phys., v.12 (4) (1967)
(Heb 2007) Hebert, A., "A Raviart-Thomas-Schneider Solution of the Diffusion Equation in Hexagonal Geometry", Annals of Nuclear Energy 35 (2008) 363-376.

(Hir 2003) Hiruta, H. and Anistratov, D. Y., "Splitting Method for Solving the Coarse-Mesh Discretized Low-Order Quasidiffusion Equations", Nuclear Mathematical and Computational Sciences: A Centenary in Review, a Century Anew Gatlinburg, Tennessee, April 6-11, 2003, on CD-ROM, American Nuclear Society, La Grange Park, IL (2003)

(Law 1986) Lawrence, R.D., "Progress in Nodal Methods for the Solutions of the Neutron Diffusion and Transport Equations", *Progress in Nuclear Energy*, Vol.17, No.3, pp.271-301 (1986)

(Lew 1993) Lewis, E.E. and Miller, W.F Jr., "Computational Methods of Neutron Transport", American Nuclear Society, Inc., La Grange Park, Illinois (1993)

(McGhee 2009) McGhee, J.M. et al, "Attila User's Manual", Transpire. Inc., Gig Harbor, WA, November 2, 2009.

(Mif 1993) Miften, M.M. and Larsen, E.W., "A Symmetrical Quasidiffusion Method for solving Transport Problems in Multidimensional Geometries", Proc. ANS Topical Meeting, *Mathematical Methods and Supercomputing in Nuclear Applications, M&C+SNA'93*, April 19-23, 1993, Karlsruhe, Germany

(Nes 2002) Nes, R and Pamer, T.S., "An Advanced Nodal Discretization for the Quasi-Diffusion Low-Order Equations", Summary submitted to the 2002 ANS RPD Topical Meeting – PHYSOR 2002, Seoul, Korea (2002)

(NRC 2013) www.nrc.gov

(Pal 2001) Palmer, T.S., Private Communication (2001)

(Pal 1997) Palmtag, S.P., "Advanced Nodal Methods for MOX Fuel Analysis", PhD Thesis, Massachusetts Institute of Technology (1997)

(Rad 1992) Rade, L. and Westergren, B., "Beta Mathematics Handbook", CRC Press, Boca Raton (1992)

(Sci 2009) www.sciencedirect.com

(Smi 1986) Smith, K.S., “Assembly Homogenization Techniques for light Water Reactor Analysis”, *Progress in Nuclear Energy,* Vol.17, No.3, pp.303-305 (1986)

(Sta 2007) Stacey, W. M., "Nuclear Reactor Physics", Wiley-VCH Verlag GmbH&Co KGaA, 2007

(Stu 2013) www.stutsvikscandpower,com

(Wha 2013) www.whatisnuclear.com